J. Fluid Mech. (1992), *vol.* 235, *pp.* 611–642
Printed in Great Britain

The influence of viscoelasticity on the existence of steady solutions in two-dimensional rimming flow

By DILIP RAJAGOPALAN,[1] RONALD J. PHILLIPS,[1] ROBERT C. ARMSTRONG,[1] ROBERT A. BROWN[1] AND ARIJIT BOSE[2]

[1] Department of Chemical Engineering, Massachusetts Institute of Technology, Cambridge, MA 02139, USA

[2] Department of Chemical Engineering, University of Rhode Island, Kingston, RI 02881, USA

(Received 5 October 1990 and in revised form 15 August 1991)

The steady, two-dimensional flows and interface shapes of the rimming flow of Newtonian and viscoelastic liquid films are studied by finite-element analysis. The viscoelastic flow calculations are based on the elastic–viscous split stress (EVSS) formulation for differential constitutive models. The EVSS formulation is derived by taking into account the mathematical type of the momentum, continuity and constitutive equations and is extended in this paper to calculation of free-surface flows. Calculations for a viscous Newtonian fluid demonstrate the balance between viscous forces and gravity which sets the shape of the interface of the liquid film coating the inside of the rotating cylinder. The liquid shape evolves from a concentric and circular film at high rotation rates to become thicker on the rising surface as the rotation rate is lowered. No steady flows with continuous films are found to exist below a minimum rotation rate, $\Omega = \Omega_c$, where the family of flows evolves back toward higher values of Ω. Multiple solutions are predicted for a range of rotation rates, $\Omega > \Omega_c$, and unstable flows develop a pronounced bulge on the rising side of the film. Asymptotic analysis for a thin film predicts this limiting rotation rate. Adding viscoelasticity to the liquid, as modelled by the Giesekus constitutive equation, leads to the existence of steady solutions at lower rotation rates and causes the bulge to appear on stable films. The minimum rotation rate for steady, viscoelastic flow shifts to lower values as the time constant of the fluid is increased.

1. Introduction

Polymer processing operations typically involve flows with gas/liquid and liquid/liquid free surfaces. The unit operations of coating, film blowing, fibre spinning, and injection molding are examples of such processes (Pearson 1985). Accordingly there has been a great deal of interest in numerical simulation of such flows for viscoelastic liquid and melts; see Crochet, Davies & Walters (1984) and Keunings (1989) for references. However, the development of numerical methods for viscoelastic, free-surface flows has been severely limited by the inherent difficulties associated with the numerical solution of any viscoelastic flow. Numerically stable and convergent algorithms have only recently been developed for finite-element computation of viscoelastic flows whose exact solutions are not smooth and contain boundary layers and/or singularities (Marchal & Crochet 1987; King *et al.* 1988; Rajagopalan, Armstrong & Brown 1990*b*). In this paper, the elastic–viscous split

stress (EVSS) formulation, developed by Rajagopalan *et al.* (1990*b*) for differential constitutive models, is extended to the calculation of viscoelastic, free-surface flows.

The calculations presented here are for steady, two-dimensional flow in a liquid film on the inside of a long, horizontal, rotating cylinder. The film is dragged around with the cylinder by shear forces, and its motion is resisted by gravity on the rising side of the cylinder. At high rotation rates, the film is in rigid motion and the gas/liquid interface is perfectly cylindrical, centred inside the containing cylinder. The flow deviates from rigid motion as the rotation rate of the cylinder is lowered. At low rotation rates no continuous film is expected, because the liquid will fall from the top of the cylinder and shear forces will be insufficient to drag the fluid from the bottom.

This so-called 'rimming' flow has been studied by several researchers by both asymptotic and numerical analysis for a Newtonian fluid, and their results are the starting point for the analysis of the viscoelastic flow. For several reasons, rimming flow is an ideal problem for understanding the effect of elasticity on a viscous, free-surface flow. First, for continuous liquid films, there are no contact lines between the gas/liquid interface and the solid. The importance of these contact lines is just beginning to be understood, even for Newtonian flows. Also, there is mounting evidence that the mathematical singularities introduced in the stress and pressure fields near these contact lines can have a drastic effect on the solvability of viscoelastic flows, depending on the asymptotic behaviour of the constitutive equation in this region (Apelian, Armstrong & Brown 1988; Coates, Armstrong & Brown 1992). Furthermore, the periodic nature of the problem in the azimuthal direction eliminates the need for inflow/outflow boundary conditions. The absence of these difficulties in the analysis of rimming flow was one of the reasons why this problem was selected by Orr & Scriven (1978) for one of the first numerical calculations of a Newtonian, free-surface flow.

The rimming flow problem is particularly convenient for theoretical analysis, because both Newtonian and viscoelastic flows approach rigid rotation in the limit of very high rotation rates. This limit was the starting point of the asymptotic analysis of Ruschak & Scriven (1976), who presented a regular perturbation solution in terms of the inverse Froude number, $g \equiv G/\Omega^2 R_c$, where G is the gravitational acceleration, Ω is the rotation rate of the cylinder, and R_c is its radius. They derived several parametric limits of their perturbation solution. One such limit was for small fluid inertia (low Reynolds number) and thin liquid films which was the lubrication limit considered earlier by Rao & Thorne (1972) in an analysis of rotational molding. The case of high Reynolds number, where viscous forces are confined to a thin boundary layer adjacent to the solid cylinder, was also considered by Ruschak & Scriven.

Johnson (1988) used lubrication analysis in a study of rimming flow for both continuous and discontinuous thin films of Newtonian and generalized-Newtonian (power-law) fluids. He showed that two types of continuous film profiles are possible. The first corresponds to film depths that change smoothly around the cylinder and are thicker on the ascending portion and thinner on the descending side. The second type of film profile has rapid changes in the film depth on the rising side of the cylinder, where flow recirculation is possible. Johnson does not comment on the stability or connectivity of these two types of solution profiles. We demonstrate by a set of calculations that smoothly varying films and films with extreme bulges on the rising side of the cylinder are connected through folds in the solution surface as the rotation rate is varied.

Orr & Scriven (1978) presented numerical simulations of Newtonian rimming flow in their development of finite-element methods for viscous, free-surface flows. Their calculations were compared directly to the perturbation results of Ruschak & Scriven (1976) as a test of accuracy. We present similar calculations in §4.1 as a test of our numerical analysis.

The only previous study of viscoelastic rimming flow is the regular perturbation analysis of Sanders, Joseph & Beavers (1981) which is based on an expansion in a small parameter analogous to the inverse Froude number g. This theory is developed for a general fluid with memory (Green & Rivlin, 1957) and relates the complex viscosity of the fluid to the film profile for $g \ll 1$. The asymptotic analysis was coupled with experimental measurements of the liquid film profile at various rotation rates to determine the fluid's complex viscosity, thereby characterizing its linear viscoelastic behaviour. Sanders *et al.* also observed instabilities in the film that developed as the rotation rate was decreased: the two-dimensional film first became unstable to a fully three-dimensional cellular pattern. Similar patterns were seen for viscous Newtonian liquids, and the authors concluded that the instability was not greatly influenced by the non-Newtonian character of the fluid. However, based on the experimental observations of Deiber & Cerro (1976), and Karweit & Corrsin (1975) with low-viscosity liquids, Sanders *et al.* suggest that there is a qualitative difference in the stability of rimming flow of high- and low-viscosity fluids.

The numerical simulation of viscoelastic, free-surface flows has received limited attention because of the difficulties associated with developing convergent calculations for much simplier viscoelastic flows. The initial attempts at the numerical simulation of viscoelastic flow all suffered the so-called 'high Deborah number problem' (Brown *et al.* 1986; Keunings 1989). The calculations failed to converge for flows with appreciable elasticity and were not convergent with refinement of the numerical discretization; the calculations reached ever-decreasing values of elasticity as the mesh was refined. Moreover, the solutions developed mesh-sized oscillations that were indicative of a Hadamard instability in an improperly formulated numerical discretization. Of the attempts at solution of viscoelastic, free-surface flows, only the calculations of Keunings and co-workers (Keunings 1986; Keunings & Bousfield 1987; Bousfield *et al.* 1986; Musarra & Keunings 1989) appear to be free of numerical instability. However, as pointed out by Keunings (1989, p. 421), this may be attributable to the fact that the flows computed in these studies had smooth exact solutions, without any boundary layers or singularities.

The breakthrough in the formulation of appropriate numerical methods for viscoelastic flows was prompted by a mixture of theory and numerical experiments. The theoretical work of Joseph, Renardy & Saut (1985) showed that the equation set formed from the momentum/continuity pair and a typical differential constitutive equation is of mixed hyperbolic and elliptic character for steady flows. For a general class of constitutive equations, the momentum/continuity pair is an elliptic saddle point problem for the velocity and pressure fields, and the components of the constitutive equation are a set of first-order hyperbolic equations for the stress. Conventional Galerkin finite-element methods applied to hyperbolic equations were known to be inaccurate and sometimes unstable, especially for singular problems (Brooks & Hughes 1982). The need to modify the discretization of the constitutive equation and utilize upwinding techniques to stabilize the numerical algorithm was recognized by Marchal & Crochet (1987) and by King *et al.* (1988).

Marchal & Crochet (1987) developed a finite-element formulation that uses streamline upwinding (Brooks & Hughes 1982) to stabilize the discretization of the

constitutive equation. Streamline upwinding is analogous to the artificial diffusion used to stabilize finite-difference discretizations of hyperbolic problems. Marchal & Crochet were able to reach high Deborah numbers in viscoelastic flow calculations, without numerical instabilities. Dheur & Crochet (1989) extended the analysis to stratified flows with liquid/liquid free surfaces. The formulation of Marchal & Crochet yielded calculations to high Deborah number; however the application of streamline upwinding yields stresses that are at most first-order accurate. This first-order rate of convergence is apparent in the recent comparison (Crochet, Delvaux & Marchal 1990) between results obtained with this method and with the highly accurate spectral calculations presented by Pilitsis & Beris (1989) for viscoelastic flow through a corrugated tube.

The explicitly elliptic momentum equation (EEME) formulation was proposed by King *et al.* (1988) for calculation of viscoelastic flows using the upper-convected Maxwell (UCM) model. This formulation is successful for two main reasons. First, when the governing equations for viscoelastic flow are in EEME form, the momentum equation contains an explicit, generalized Stokes operator, which is guaranteed to be elliptic for all inertialess flows. The explicitly elliptic saddle point problem for velocity and pressure are solved by finite-element methods appropriate for generalized Stokes problems (Carey & Oden 1986). Second, the constitutive equation is discretized using the high-order-accurate streamline-upwind/Petrov–Galerkin (SUPG) method, developed by Brooks & Hughes (1982). The near optimal convergence rate of the SUPG method for linear, hyperbolic problems was established by Johnson, Navert & Pitkaranta (1984). King *et al.* (1988) and Burdette *et al.* (1989) have demonstrated the convergence and accuracy of the EEME formulation for model viscoelastic flows. The EEME method was extended to time-dependent flows by Northey, Armstrong & Brown (1990).

Although the EEME formulation was successful in the calculation of several viscoelastic flows using the UCM model, it is not easily extended to other constitutive models. Most of these models are either too complex to enable the derivation of the EEME, or the ellipticity of the characteristics associated with the momentum equation cannot be guaranteed. However, the methodology used to construct the EEME formulation is robust. The idea is to construct numerical algorithms based on reformulated governing equations that contain dominant and explicit differential operators in each equation and to use discretization methods that respect the mathematical type of these equations. This methodology has lead to another numerical formulation that is applicable to a wide variety of constitutive models. This new formulation hinges on decomposing the stress tensor into Newtonian and elastic contributions. When this decomposition is substituted into the governing equations, a dominant, explicitly elliptic operator appears in the momentum equation. We call this method the elastic–viscous split stress (EVSS) formulation; the finite-element algorithms based on this method and sample test calculations, for flows without geometric singularities, are described in Rajagopalan *et al.* (1990*b*). These results demonstrate the high-order accuracy of the EVSS method and excellent agreement with the spectral calculations of Pilitsis & Beris (1989) up to high Deborah number.

In this paper, we present an extension of the EVSS/finite-element method to viscoelastic, free-surface flows. This extension is based on well-developed finite-element methodology for Newtonian, free-surface flows. In this framework, the shear and normal stress boundary conditions along the free surface are naturally incorporated into the weak form of the momentum equation. The free-interface

shape is discretized by one-dimensional approximating functions, and the kinematic condition at the interface is used to determine the location of the surface. The weak formulation yields a large set of nonlinear, algebraic equations in terms of the finite-element expansion coefficients of the field variables and the interface shape. This equation set is solved by Newton's method where the Jacobian matrix represents the sensitivity of the equations to changes in field variables and the surface shape (Kistler & Scriven 1983). Variations in the shape or position of the free-surface change the finite-element mesh, which in turn influences the approximation of the field variables. This effect is explicitly accounted for in the Jacobian matrix.

The calculations presented here are based on a simple Mongé representation (Weatherburn 1927) of the gas/liquid interface. The distances of the interface from the the centre of the cylinder at a set of azimuthal locations are used to represent the free surface. The calculations are limited to surface shapes that are single-valued in this representation, i.e. the surface can nowhere be tangent to a line drawn radially outward from the centre of the cylinder. Although this constraint is not restrictive for calculation of Newtonian flows, viscoelastic flows exhibit a tendency to form exaggerated bulges which violate this criterion.

The viscoelastic flow simulations presented here are carried out using a single-mode Giesekus differential constitutive equation to model the polymeric part of the deviatoric stress along with an additional Newtonian contribution to the stress tensor that accounts for the presence of a solvent. This constitutive equation is representative of a large class of models based on the UCM equation, so the calculations demonstrate the applicability of the numerical method to these models. The model parameters used are appropriate for a polymer solution described in detail by Quinzani *et al.* (1990). This solution of high-molecular-weight polysiobutylene in a polybutene/tetradecane solvent is called a 'Boger' fluid.

The formulation of the Newtonian and viscoelastic rimming flow problem is described in §2. The EVSS/finite-element method for the free-surface flow is presented in §3. Results for both Newtonian and viscoelastic flows are described in §4 and are compared in §5 with a simple lubrication analysis for Newtonian flow.

2. Flow geometry and governing equations

The analysis is for a long, horizontal, cylinder of inner radius R_c, rotating at an angular velocity Ω. The cylinder is rotated fast enough that, when partially filled with a liquid of density ρ, the liquid forms a continuous film that completely wets the cylinder. The gaseous core is assumed to be inviscid and to exert only an isotropic pressure on the liquid film. The calculations are for steady, two-dimensional, continuous liquid films with specified liquid volumes per unit length of the cylinder. Physically, this system would correspond to sealing the ends of the cylinder from the ambient, so that pressure in the gas core is unknown. A cross-section of the flow geometry is represented in figure 1.

The flow field and interface shape are represented in a cylindrical polar coordinate system (r, θ) centred on the axis of the cylinder. Natural length and velocity scales for the flow are the cylinder radius R_c and the linear velocity of the cylinder ΩR_c, respectively. The location of the interface between the liquid and gas is given by the dimensionless shape function $r = h(\theta)$. In the absence of gravitational acceleration, the interface is concentric with the cylinder, and $h(\theta)$ is a constant determined solely by the volume of liquid loaded into the cylinder. The unit outward normal to the

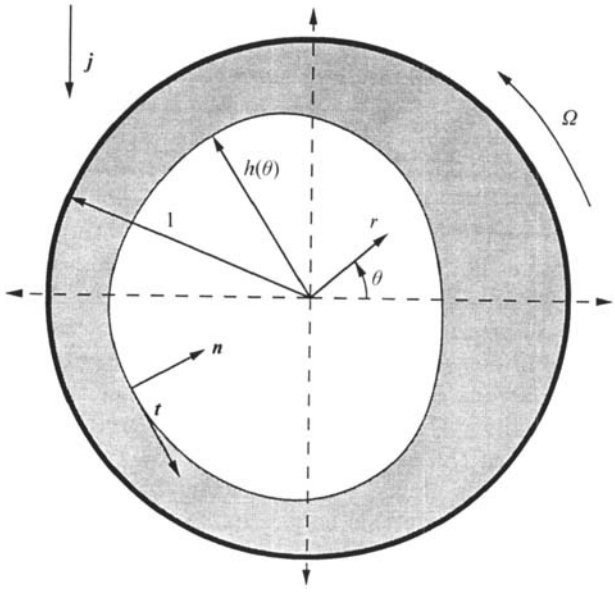

FIGURE 1. The rimming flow geometry.

interface $\boldsymbol{n}$ and the unit tangent vector $\boldsymbol{t}$ are shown in figure 1 and are expressed in terms of $h(\theta)$ as

$$\boldsymbol{n} = \frac{-h\boldsymbol{e}_r + (\mathrm{d}h/\mathrm{d}\theta)\,\boldsymbol{e}_\theta}{[(\mathrm{d}h/\mathrm{d}\theta)^2 + h^2]^{\frac{1}{2}}}, \tag{1}$$

$$\boldsymbol{t} = \frac{h\boldsymbol{e}_\theta + (\mathrm{d}h/\mathrm{d}\theta)\,\boldsymbol{e}_r}{[(\mathrm{d}h/\mathrm{d}\theta)^2 + h^2]^{\frac{1}{2}}}; \tag{2}$$

where $\boldsymbol{e}_i$ is the unit vector in the ith coordinate direction.

The conservation equations for the liquid phase are given in dimensionless form as

$$\nabla \cdot \boldsymbol{v} = 0, \tag{3}$$

$$\boldsymbol{v} \cdot \boldsymbol{q}\nabla \boldsymbol{v} + \nabla \cdot \boldsymbol{\pi} - g\boldsymbol{j} = 0, \tag{4}$$

where $\boldsymbol{v}$ is the velocity vector, $\boldsymbol{\pi}$ is the total stress tensor, made dimensionless by using the inertial scale $\rho\Omega^2 R_c^2$, $\boldsymbol{j}$ is the unit vector pointing vertically downward in the direction of gravity; and $g \equiv G/\Omega^2 R_c$ is the dimensionless gravitational acceleration or inverse Froude number.

The stress tensor is decomposed into the isotropic pressure $p(r, \theta)$ and the deviatoric stress tensor $\boldsymbol{\tau}$ as

$$\boldsymbol{\pi} \equiv p\boldsymbol{I} + \boldsymbol{\tau} \tag{5}$$

The description of the fluid phase is completed by a constitutive equation for $\boldsymbol{\tau}$. For the Newtonian fluid of viscosity μ, $\boldsymbol{\tau}$ is given by

$$\boldsymbol{\tau} \equiv -\frac{1}{Re}\dot{\boldsymbol{\gamma}}, \tag{6}$$

where $\dot{\boldsymbol{\gamma}} \equiv (\nabla \boldsymbol{v}) + (\nabla \boldsymbol{v})^{\mathrm{T}}$ is the rate-of-strain tensor, and the Reynolds number is $Re \equiv \rho\Omega R_c^2/\mu$.

Viscoelastic flow calculations are based on the single-mode, nonlinear constitutive equation developed by Giesekus (1982) and described in an augmented form by Bird,

Armstrong & Hassager (1987). The Giesekus model is best written by dividing the deviatoric stress into a Newtonian solvent contribution $\boldsymbol{\tau}_s$ and a viscoelastic contribution $\boldsymbol{\tau}_p$ as

$$\boldsymbol{\tau} \equiv \boldsymbol{\tau}_s + \boldsymbol{\tau}_p. \tag{7}$$

The two components of $\boldsymbol{\tau}$ are given in dimensionless form by

$$\boldsymbol{\tau}_s \equiv -\frac{\beta}{Re}\dot{\boldsymbol{\gamma}}, \tag{8}$$

and

$$\boldsymbol{\tau}_p + De\,\boldsymbol{\tau}_{p(1)} - \frac{\alpha\, De\, Re}{(1-\beta)}\{\boldsymbol{\tau}_p \cdot \boldsymbol{\tau}_p\} + \frac{(1-\beta)}{Re}\dot{\boldsymbol{\gamma}} = 0, \tag{9}$$

where $\boldsymbol{\tau}_{p(1)}$ is the upper-convected derivative of $\boldsymbol{\tau}_p$. For steady flow, $\boldsymbol{\tau}_{p(1)}$ is

$$\boldsymbol{\tau}_{p(1)} \equiv \boldsymbol{v}\cdot\nabla\boldsymbol{\tau}_p - (\nabla\boldsymbol{v})^{\mathrm{T}}\cdot\boldsymbol{\tau}_p - \boldsymbol{\tau}_p\cdot(\nabla\boldsymbol{v}). \tag{10}$$

The three parameters appearing in the Giesekus model (8)–(9) are: the dimensionless viscoelastic relaxation time or the Deborah number $De \equiv \lambda\Omega$, where λ is the dimensional relaxation time; the mobility parameter α, which is a measure of the importance of anisotropic hydrodynamic drag on the macromolecules; and β, the ratio of the solvent viscosity (η_s) to the total zero-shear-rate viscosity of the polymer solution (η_0). The solution viscosity (η_0) is defined as the sum of the solvent viscosity and the zero-shear-rate viscosity of the polymer (η_p). Hence, β is

$$\beta \equiv \frac{\eta_s}{\eta_0} = \frac{\eta_s}{\eta_s + \eta_p}. \tag{11}$$

The Reynolds number in (9) is defined in terms of the solution viscosity as $Re \equiv \rho\Omega R_c^2/\eta_0$.

The Giesekus model is one of the simplest differential constitutive equations that qualitatively describes the rheological behaviour of polymer solutions (Bird *et al.* 1987). It predicts shear-thinning viscosity and first-normal stress coefficient as a function of shear rate, and bounded extensional viscosities as a function of extension rate. Moreover, multimode extensions of the Giesekus model that include a spectrum of relaxation times have been used to fit quantitatively the rheological data for several polyisobutylene solutions (Quinzani *et al.* 1990). In the limit of vanishing mobility, $\alpha = 0$, the Giesekus model reduces to the Oldroyd-B model, and when $\alpha = \eta_s = 0$, the UCM model is obtained. Both of these models fail to predict shear-thinning rheological properties in steady-shear flow and both predict unbounded extensional viscosities at finite extension rates.

The problem statement is completed by setting boundary conditions at the cylinder surface and the gas/liquid interface. At the cylinder surface, the no-slip and no-penetration conditions yield

$$\boldsymbol{v} = \boldsymbol{e}_\theta \quad r = 1, \quad 0 \leqslant \theta \leqslant 2\pi. \tag{12}$$

At the gas/liquid interface ($r = h(\theta)$, $0 \leqslant \theta \leqslant 2\pi$) the kinematic constraint requires that no liquid cross the interface, i.e.

$$\boldsymbol{v}\cdot\boldsymbol{n} = 0. \tag{13}$$

The stress balance at the interface is decomposed into shear

$$\boldsymbol{t}\boldsymbol{n}:\boldsymbol{\pi} = 0 \tag{14}$$

and normal components

$$\boldsymbol{nn}:\boldsymbol{\pi}-p_g+2\mathscr{H}We=0 \tag{15}$$

where $\mathscr{H}$ is the local mean curvature of the interface and the Weber number $We \equiv \sigma/\rho\Omega^2 R_c^3$ scales the importance of the surface tension (σ) relative to the fluid inertia.

The pressure in the gas core (p_g) in (15) is computed so that the constraint of fixed liquid volume per unit length (V)

$$\frac{1}{2}\int_0^{2\pi} h^2\,\mathrm{d}\theta = \pi - V \tag{16}$$

is satisfied.

In addition to the boundary conditions (12)–(15), all field variables and the interface shape must be 2π-periodic in the azimuthal coordinate. Also, an arbitrary datum pressure is set in the liquid as $p(1, 0) = 0$ to specify completely the pressure in the momentum equation. An alternative formulation used by Sackinger, Brown & Derby (1989) is to set the gas pressure arbitrarily and use the volume constraint (16) to compute a datum pressure difference across the interface.

3. Numerical method

The finite-element analysis of the viscoelastic rimming flow problem, (2)–(16), is based on the extension of the EVSS method of Rajagopalan *et al.* (1990*b*) to account for the free surface. The solution of the purely Newtonian problem is recovered in the limit $De = 0$, and so its formulation is not presented separately.

The EVSS method for viscoelastic flows is based on splitting the stress into elastic and viscous contributions. Substituting this splitting into the governing equations yields a dominant, explicitly elliptic operator on velocity in the momentum equation. The EVSS reformulation is implemented by defining the elastic stress tensor $\boldsymbol{\Sigma}(r, \theta)$ as

$$\boldsymbol{\Sigma} \equiv \boldsymbol{\tau}_p + \frac{(1-\beta)}{Re}\dot{\boldsymbol{\gamma}}. \tag{17}$$

Using (17) to eliminate $\boldsymbol{\tau}_p$ from the deviatoric stress (7) and substituting into the expression for the total stress (5) leads to the stress tensor ($\boldsymbol{\pi}$) defined as

$$\boldsymbol{\pi} \equiv p\boldsymbol{I} + \boldsymbol{\Sigma} - \dot{\boldsymbol{\gamma}}/Re. \tag{18}$$

The EVSS form of the governing equations is obtained by substituting (18) into the momentum equation (4) and by using (17) to eliminate $\boldsymbol{\tau}_p$ from the constitutive equation for the polymeric part of the stress, (9). For steady flows, these equations are

$$\boldsymbol{\nabla}\cdot\boldsymbol{v} = 0, \tag{19}$$

$$\boldsymbol{v}\cdot\boldsymbol{\nabla}\boldsymbol{v} + \boldsymbol{\nabla}\cdot(p\boldsymbol{I} + \boldsymbol{\Sigma} - \dot{\boldsymbol{\gamma}}/Re) - g\boldsymbol{j} = 0, \tag{20}$$

$$\boldsymbol{\Sigma} + De\boldsymbol{\Sigma}_{(1)} - \frac{\alpha\, De\, Re}{(1-\beta)}\boldsymbol{\Sigma}\cdot\boldsymbol{\Sigma} - \frac{(1-\beta)\,De}{Re}\dot{\boldsymbol{\gamma}}_{(1)} - \frac{\alpha\, De\,(1-\beta)}{Re}\dot{\boldsymbol{\gamma}}\cdot\dot{\boldsymbol{\gamma}} + \alpha De(\boldsymbol{\Sigma}\cdot\dot{\boldsymbol{\gamma}} + \dot{\boldsymbol{\gamma}}\cdot\boldsymbol{\Sigma}) = \boldsymbol{0}, \tag{21}$$

where the dependent variables are now ($\boldsymbol{v}$, $\boldsymbol{\Sigma}$, p). It is important to note that the components of $\dot{\boldsymbol{\gamma}}_{(1)}$ in (21) contain second-order derivatives of the velocity field. These terms will require special consideration in the numerical formulation.

Equations (19)–(21) and the reformulated boundary conditions are discretized and solved by using the finite-element method. The dependent variables are expanded in classical Lagrangian basis functions which have compact support over the domain and are only $\mathscr{C}_0$ continuous across interelement boundaries (Strang & Fix 1973). The choices of the polynomials and the methods for discretization and incorporation of the boundary conditions hinge on the mathematical type of (19)–(21). The continuity and momentum equations, (19) and (20), form an elliptic saddle point problem for the velocity and pressure that is a straightforward generalization of the saddle point problem for Stokes flow (Carey & Oden 1986). We discretize these equations by a mixed, finite-element method for velocity and pressure that is proven convergent for Newtonian flows. Here the velocity components are represented by expansions in biquadratic basis functions $\phi_i^V(r, \theta)$ and the pressure by an expansion in bilinear functions $\phi_i^P(r, \theta)$. Galerkin's method is used to discretize these equations, as described below.

Consistent with these approximations, the liquid region is subdivided into isoparametric elements. The meshes have rows of elements aligned with the gas/liquid interface and are defined by the number of elements in the radial (N_r) and azimuthal (N_θ) directions. Unless otherwise stated, the elements are uniformly distributed in both directions. The interface shape is approximated by one-dimensional Lagrangian quadratic functions $\psi_i^H(\theta)$.

The constitutive equation (21) is hyperbolic in the elastic stress ($\boldsymbol{\Sigma}$). We discretize this equation by the SUPG method, which is proven convergent for linear hyperbolic equations (Johnson *et al.* 1984). Biquadratic polynomials $\phi_i^S(r, \theta)$ are used to approximate the stress components. Because the finite-element representation of the velocity field is only $\mathscr{C}^0$-continuous at interelement boundaries, the second derivatives of velocity that appear in the term $\dot{\boldsymbol{\gamma}}_{(1)}$ are ill-defined on these boundaries. As described in Rajagopalan *et al.* (1990*b*), we eliminate these singularities by interpolating the independent components of the rate-of-strain tensor ($\dot{\boldsymbol{\gamma}}$) onto a continuous bilinear representation by the least-squares method. The weak form of the interpolation condition is

$$\int_{\mathscr{D}} \{\dot{\boldsymbol{\gamma}} - (\boldsymbol{\nabla v}) - (\boldsymbol{\nabla v})^{\mathrm{T}}\} \phi_i^G \, \mathrm{d}A = 0, \tag{22}$$

where $\phi_i^G(r, \theta)$ denotes the basis functions for the rate of strain and the integral is over the liquid ($\mathscr{D}$). The term $\dot{\boldsymbol{\gamma}}_{(1)}$ is written in terms of first derivatives of the rate-of-strain tensor, which are well-defined across interelement boundaries.

The weak forms of the momentum equation and the boundary conditions (13)–(15) along the interface deserve special mention, because these conditions determine both the velocity field *and* the free surface shape. Following the finite-element algorithm developed by Kistler & Scriven (1983), we distinguish the kinematic condition (13) as the explicit equation for the interface shape and incorporate the normal (equation (15)) and shear (equation (14)) stress balances into the weak form of the momentum equation.

A residual equation for the kinematic condition is formed by Galerkin's method by using the basis functions for the free surface as

$$\int_{\delta\mathscr{D}_1} (\boldsymbol{v} \cdot \boldsymbol{n}) \psi_i^H \, \mathrm{d}s = 0, \tag{23}$$

where the integral is over the free surface $\delta\mathscr{D}_1$.

The weak form of the momentum equation is developed by using the typical procedure for Newtonian flows (Carey & Oden 1986). The divergence theorem is applied to the Galerkin weighted residual equations to yield

$$\int_{\mathscr{D}} \{\phi_i^V (\boldsymbol{v}\cdot\nabla\boldsymbol{v} - g\boldsymbol{j})\cdot\boldsymbol{e}_k - \phi_i^V\, \boldsymbol{\pi}:\nabla\boldsymbol{e}_k - \nabla\phi_i^V\cdot(\boldsymbol{\pi}\cdot\boldsymbol{e}_k)\}\,\mathrm{d}A + \int_{\phi\mathscr{D}} (\phi_i^V\, \boldsymbol{n}\cdot\boldsymbol{\pi}\cdot\boldsymbol{e}_k)\,\mathrm{d}s = 0, \tag{24}$$

where $\delta\mathscr{D}$ is the entire boundary including the solid surface of the cylinder and the artificial boundaries at $\theta = 0$ and $\theta = 2\pi$.

The boundary conditions are applied directly to the weak form (24). The boundary integral in this equation is split into contributions from each segment of the boundary. The contribution from the solid surface is unimportant because the components of the momentum equation along that boundary are replaced by the essential boundary conditions on velocity given by (12). The contributions along the periodic segments cancel each other because all variables have the same values and the outward normal points in opposite directions, depending on whether the segment is viewed from $\theta = 0$ or $\theta = 2\pi$. The only remaining contribution is evaluated along the free surface where the components of the stress balance are applied. The integrand in the boundary integral in (24) is rewritten in terms of the shear, (14), and normal stress, (15), conditions as

$$\boldsymbol{n}\cdot\boldsymbol{\pi} = (\boldsymbol{nn}:\boldsymbol{\pi})\,\boldsymbol{n} + (\boldsymbol{tn}:\boldsymbol{\pi})\boldsymbol{t} = (p_g - 2\mathscr{H}We)\,\boldsymbol{n}. \tag{25}$$

The local mean curvature $2\mathscr{H}$ is expressed in terms of the surface derivative of the local tangent vector (Weatherburn 1927) as

$$2\mathscr{H}\boldsymbol{n} = \frac{\mathrm{d}\boldsymbol{t}}{\mathrm{d}s}, \tag{26}$$

where s is the arclength along the surface. Substituting (26) into (25) yields

$$\boldsymbol{n}\cdot\boldsymbol{\pi} = p_g\,\boldsymbol{n} - We\frac{\mathrm{d}\boldsymbol{t}}{\mathrm{d}s}. \tag{27}$$

Inserting (27) into the boundary integral and integrating by parts the term $\mathrm{d}\boldsymbol{t}/\mathrm{d}s$ leads to

$$\int_{\delta\mathscr{D}_1} \phi_i^V (\boldsymbol{n}\cdot\boldsymbol{\pi}\cdot\boldsymbol{e}_k)\,\mathrm{d}s = \int_{\delta\mathscr{D}_1} \left\{\phi_i^V \left(p_g\boldsymbol{n}\cdot\boldsymbol{e}_k + We\frac{\mathrm{d}\boldsymbol{e}_k}{\mathrm{d}s}\cdot\boldsymbol{t}\right) + We\frac{\mathrm{d}\phi_i^V}{\mathrm{d}s}\,\boldsymbol{t}\cdot\boldsymbol{e}_k\right\}\mathrm{d}s. \tag{28}$$

Substituting (18) and (28) into (20) gives the weak form of the momentum equation in terms of the dependent variables ($\boldsymbol{v}$, p, $\boldsymbol{\Sigma}$, $\dot{\gamma}$, h, p_g). The gas pressure appears in the boundary integral (28) and is computed by incorporating the volume constraint, (16), as an additional constraint.

The integrals in the weak equations are evaluated by using four-point tensor product Gaussian quadrature (Strang & Fix 1973). The resulting set of nonlinear, algebraic equations are solved by Newton's method. The terms in the Jacobian matrix are evaluated by using a one-sided, finite-difference approximation, which does not significantly impact the quadratic convergence rate of the iteration. Details on the computation of the Jacobian matrix can be found in Burdette *et al.* (1989). At each finite-element node, the derivatives of the weak equations with respect to the free-surface position are evaluated by perturbing the free-surface height by a small

amount, evaluating the resulting perturbation in radial coordinates based on the nodal distance from the surface, and calculating a set of perturbed residuals. The Jacobian entries are then evaluated by subtracting the unperturbed residuals and dividing by the magnitude of the perturbation in the free-surface position. The linear equation set at each Newton iteration is solved by using frontal elimination methods (Hood 1976) to minimize the amount of core memory required. After each Newton iteration, the new nodal values of the free-surface expansion are used to update the entire mesh.

We use Newton's method to solve the nonlinear equations mainly because of its quadratic convergence rate as well as the ability to track solution families in parameter space. When a solution family does not exhibit folds in parameter space, analytic continuation methods are sufficient to calculate the solution trajectory and generate good initial guesses for the Newton iteration. The first derivatives of the residual equations with respect to the parameter are calculated and used to estimate the solution trajectory. This approximate trajectory is then used to generate a good initial guess to the solution at a new value of the parameter (Yamaguchi, Chang & Brown 1984). At a limit point, the parametric representation of the solution breaks down, and the slope of at least one of the variables becomes infinite. As described by Yamaguchi *et al.*, the most general procedure to overcome this failure is to introduce the arclength along the solution family as a new parameter, and add an equation to compute the arclength. The augmented system of equations is solved for the new discrete variables as well as the new parameter value at a prescribed arclength away from a known solution. An initial guess for both the solution and the parameter is generated by using continuation in the arclength.

Newtonian flow calculations are performed by removing the constitutive equation and the interpolation conditions for the rate-of-strain tensor from the equation set in order to minimize the size of the discrete system.

4. Results

The Newtonian and viscoelastic rimming flow problems are defined by four (Re, V, We, g) and seven (Re, V, We, g, De, α, β) dimensional parameter spaces. Complete investigation of these problems is impractical. We divide our presentation into two parts. In the first, we establish the convergence and accuracy of the numerical method. Convergence with mesh refinement is demonstrated for both Newtonian and viscoelastic flows. For Newtonian flows, we also compare our calculations to the results of the perturbation expansion of Ruschak & Scriven (1976) and to the previous finite-element calculations of Orr & Scriven (1978). In this case, the parameters selected are the same as those used by Orr & Scriven.

The second set of simulations focuses on parameter values that are appropriate for the polyisobutylene Boger fluid whose rheology is described in detail in Quinzani *et al.* (1990). We distinguish Newtonian and viscoelastic behaviour through calculations for a Newtonian fluid with the same viscosity. The numerical study of the Boger fluid involves a small parameter space because all the dimensionless groups except the liquid volume and the parameters in the constitutive equation (α, β) scale with the rotation rate. For fixed rheological parameters that best approximate the Boger-fluid rheology, we compute steady solutions as a function of decreasing rotation rate and for different liquid volumes V. The radius of the cylinder is set at $R_c = 0.05$ m.

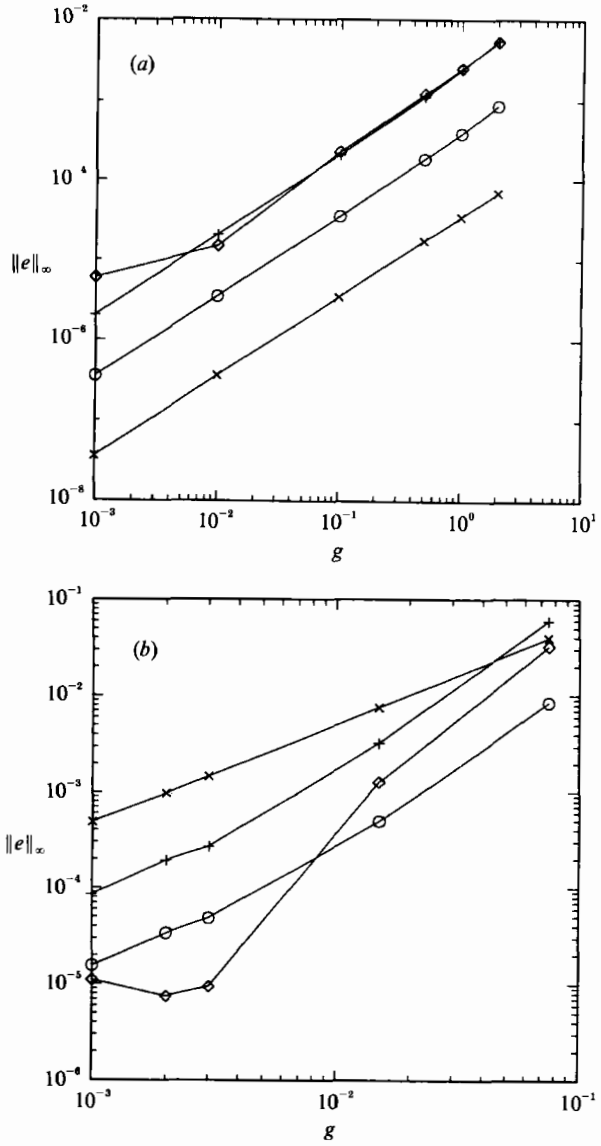

FIGURE 2. Comparison of Newtonian numerical simulation results with the perturbation solution of Ruschak & Scriven (1976); calculations are for a mesh with $(N_\theta, N_r) = 80 \times 20$, $We = 1$, and $V = 1.131$. (*a*) Low-Reynolds-number case: $Re = 1$, (*b*) high-Reynolds-number case: $Re = 1500$. +, V_θ; ×, V_r; ◇, p; ○, h.

4.1. *Accuracy and convergence*

4.1.1. *Newtonian flow*

The accuracy of the finite-element analysis for Newtonian flows is verified by direct comparison between these calculations and the results of the regular perturbation expansion in g of Ruschak & Scriven (1976). Comparisons are presented in the two limits presented by these authors: high and low Reynolds numbers. The maximum absolute difference between the finite-element and asymptotic results, $\|e\|_\infty$, is displayed in figure 2(*a*) as a function of g for each field variable: $Re = 1$, $We = 1$ and $V = 1.131$. The mesh used in this comparison had $(N_\theta, N_r) = (80, 20)$,

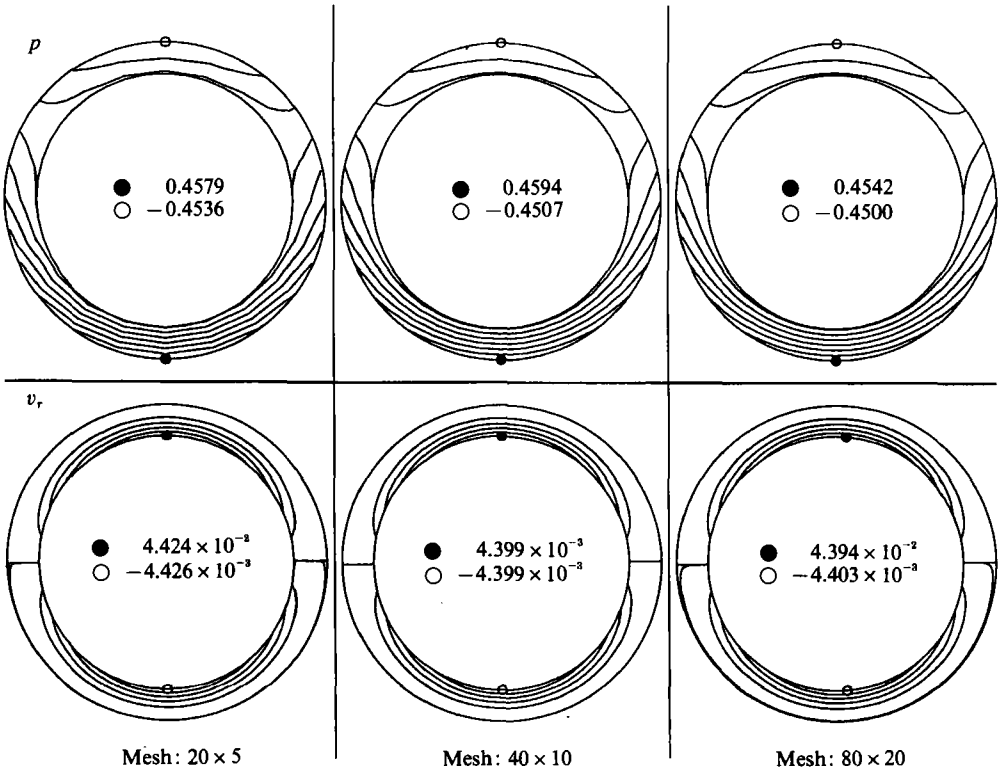

FIGURE 3. Contours of the pressure (p) and the radial velocity (v_r) for a Newtonian fluid: $g = 2$, $We = 1$, $Re = 1$, and $V = 1.131$. Results are shown for meshes with $(N_\theta, N_r) = 20 \times 5$, 40×10 and 80×20. Maximum (●) and minimum (○) values of the field are denoted.

corresponding to 14961 degrees of freedom. The agreement is very good with the largest errors appearing in the pressure and the tangential velocity. As expected, the difference between the analytical and numerical results increases with increasing g. However, there is reasonably good agreement even for $g = O(1)$, as Orr & Scriven (1978) also noticed.

Ruschak & Scriven presented inner and outer expansions of their perturbation solution for the case $Re \gg 1$. A viscous boundary layer forms adjacent to the cylinder for high Reynolds number; resolution of this layer represents a considerable challenge for the numerical computations. We have constructed the uniformly valid solution from these expansions and have compared it to the finite-element computations for $Re = 1500$, $We = 1$ and $V = 1.131$, for various values of g. A mesh of $(N_\theta, N_r) = (80, 20)$ with the radial elements graded towards the cylinder was used to capture more accurately the viscous boundary layer. Plots of the maximum difference between the computed and analytical solutions are shown in figure 2(*b*). There is good agreement in the range $10^{-3} \leqslant g \leqslant 10^{-1}$. Orr & Scriven do not show an equivalent comparison, but remark that at high Reynolds number, 'the agreement deteriorates more rapidly with increasing gravity'.

The results in figure 2 establish the accuracy of our computations on a single mesh. It is also important to demonstrate the convergence of our numerical method on successively finer meshes. The effect of mesh refinement on the calculation of the low Reynolds number ($Re = 1$) Newtonian flow is shown in figure 3; here $g = 2$, $We = 1$, and $V = 1.131$. Contours of pressure (p) and radial velocity (v_r) are shown from

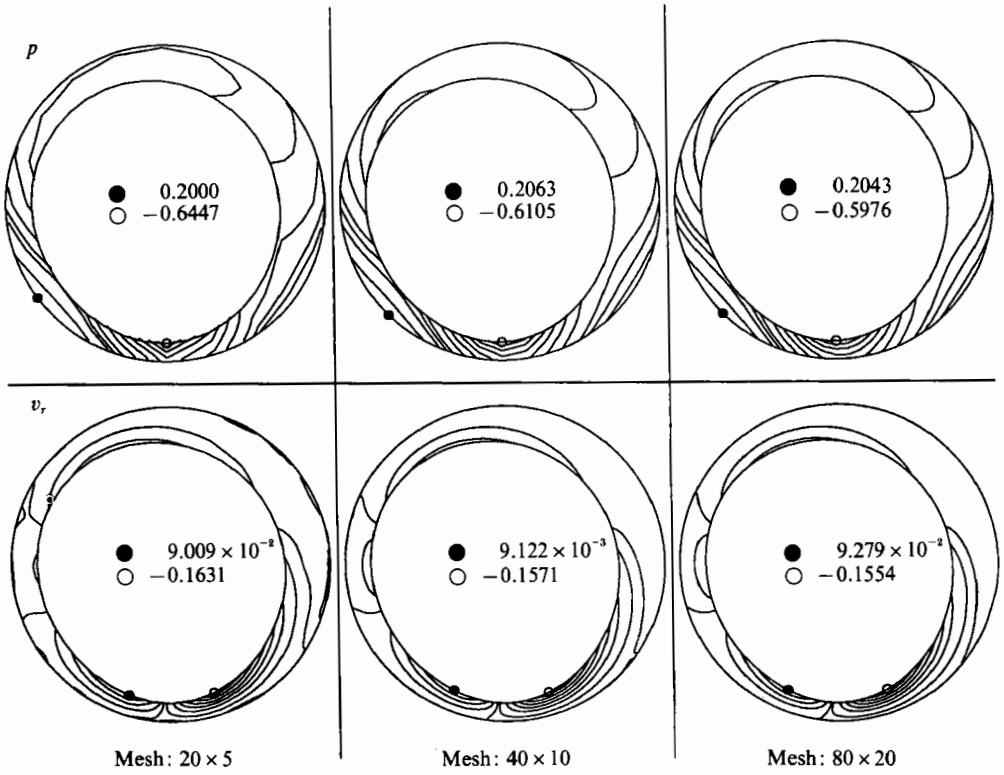

FIGURE 4. Contours of the pressure (p) and the radical velocity (v_r) for a Newtonian fluid: $g = 0.325$, $We = 1$, $Re = 150$, and $V = 1.131$. Results are shown for meshes with $(N_\theta, N_r) = 20 \times 5$, 40×10 and 80×20. Maximum (●) and minimum (○) values of the field are denoted.

calculations on three uniformly spaced meshes with $(N_\theta, N_r) = (20, 5)$, (40, 10), and (80, 20). In these contour plots, the interval between the maximum and minimum value of the field is divided into 10 equal parts and 11 contours are drawn, including the maximum and minimum values of the field. In addition, whenever the field takes on a zero value inside the domain, the zero contour is drawn for reference and is shown by a thicker curve. As the mesh is refined, the contours become smoother, and the maximum and minimum values of the fields approach constant values, indicating that the numerical method is converging.

A similar sequence of plots is shown in figure 4 for the high-Reynolds-number flow of a Newtonian fluid; $Re = 150$, $g = 0.325$, $We = 1$, and $V = 1.131$. The meshes used have the same number of elements that were used in figure 3, but each is radially graded towards the cylinder wall to capture accurately the boundary layer. The contours become smoother as the mesh is refined and the maximum and minimum values converge. The plots of the radial velocity on the two coarsest meshes show jagged zero contours at various locations in the domain. This is indicative of the solution field varying very slightly about zero. The absence of most of these contours in the calculation with the finest mesh indicates that most of these variations on the coarser meshes are a numerical artifact that is eliminated by mesh refinement.

The contours of the components of the velocity field (v_r, v_θ), pressure (p) and stream function (ψ) shown in figure 5 were computed on a mesh with $(N_\theta, N_r) = (20, 5)$ and are for exactly the same parameters for Newtonian rimming flow as used in

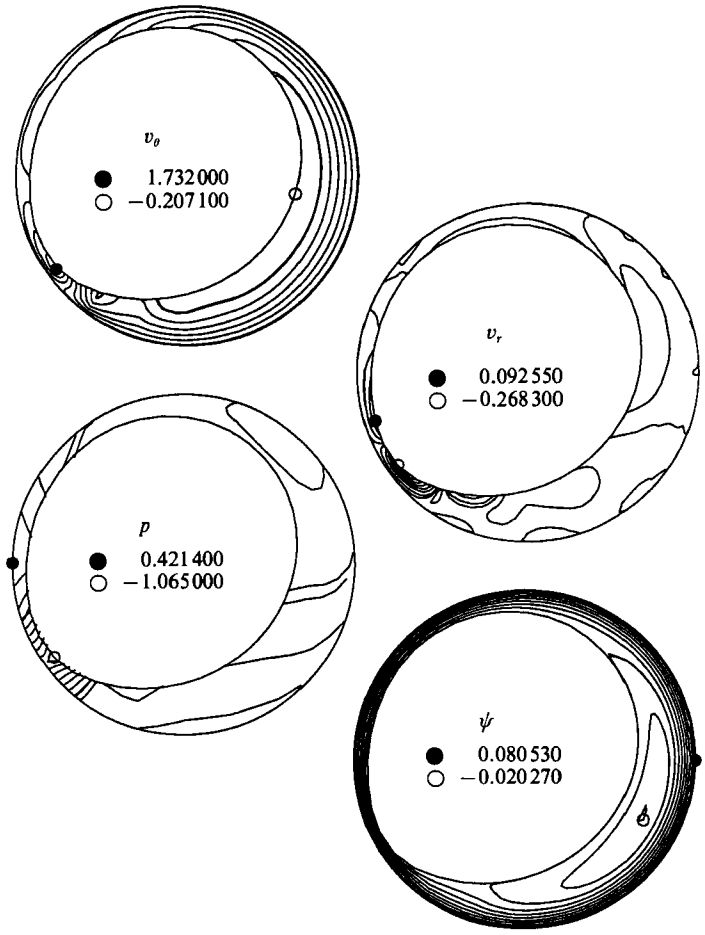

FIGURE 5. Contours of azimuthal (v_θ) and the radial (v_r) velocities, pressure (p) and stream function (ψ) for a Newtonian fluid calculated on a mesh with $(N_\theta, N_r) = 20 \times 5$: $g = 0.5$, $We = 1$, $Re = 150$, and $V = 1.131$.

figure 5 of Orr & Scriven (1978); $Re = 150$, $g = 0.5$, $We = 1$, and $V = 1.131$. There are noticeable differences between our results and those of Orr & Scriven. The shape of the free surface is obviously different as well as the size of the recirculation zone. Whereas the flow recirculation computed by Orr & Scriven is confined to the region near $\theta = \frac{3}{2}\pi$, the recirculation shown in figure 5 extends up the side of the cylinder beyond $\theta = 0$, where no backflow is observed by Orr & Scriven. This discrepancy persists on a coarser mesh comparable to the one used by Orr & Scriven, while our results compare well to the high-Reynolds-number limit of the gravity perturbation analysis, on a sequence of meshes.

4.1.2. *Viscoelastic flow*

The convergence of the EVSS/finite-element method for viscoelastic flow is established by the computation of viscoelastic rimming flow on a succession of finer meshes. In the absence of a perturbation analysis with the Giesekus model, mesh refinement is the only available test of accuracy. Convergence with mesh refinement of the EVSS formulation for the rimming flow is shown in figure 6 for the parameter

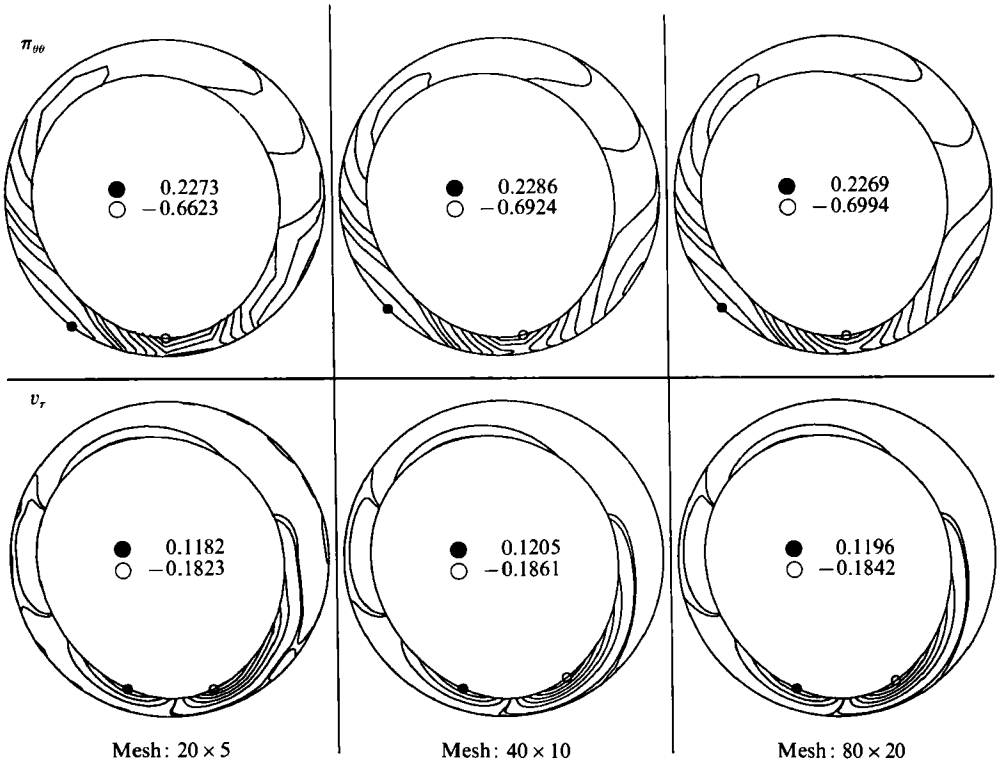

FIGURE 6. Contours of total azimuthal normal stress ($\pi_{\theta\theta}$) and the radical velocity (v_r) for a viscoelastic fluid: $g = 0.325$, $We = 1$, $Re = 150$, $V = 1.131$, $De = 1$, $\alpha = 0.01$, and $\beta = 0.5$. Results are shown for meshes with $(N_\theta, N_r) = 20 \times 5$, 40×10 and 80×20. Maximum (●) and minimum (○) values of the field are denoted.

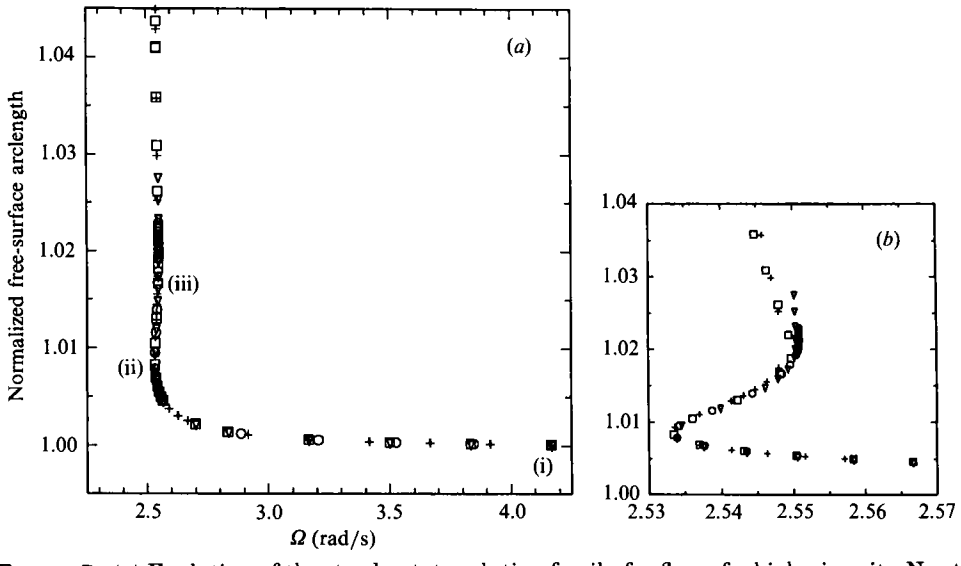

FIGURE 7. (*a*) Evolution of the steady-state solution family for flow of a high-viscosity Newtonian fluid in a 0.05 m radius cylinder. (*b*) Expanded view near the limit-point value of the rotation rate, point (ii) in (*a*). Meshes: +, 20×5; □, 40×10; ▽, 60×10; ○, 80×10.

values $Re = 150$, $g = 0.325$, $We = 1$, $V = 1.131$, $De = 1$, $\beta = 0.5$, $\alpha = 0.01$. The finite element meshes are the same as used in the computations shown in figure 4. The plots show the convergence with mesh of v_r and the azimuthal component of the total stress($\pi_{\theta\theta}$). As for the Newtonian calculations, both the form and the quantitative values of the fields converge with mesh refinement. In addition, a comparison of figures 4 and 6 shows a qualitative difference between Newtonian and viscoelastic flow. Although the gas/liquid interface is essentially circular in both cases, the interface in the viscoelastic case is rotated counterclockwise through an angle measured by the location of the maxima and minima of v_r. More examples of this phase shift are given in §4.2.

4.2. *Boger fluid calculations*

The Boger fluid calculations are for a polyisobutylene solution described by Quinzani *et al.* (1990). The rheological properties of this fluid are fit to a single-mode Giesekus model with a solvent to yield the parameters $\lambda = 0.792\ s$, $\alpha = 0.001$ and $\beta = 0.61$. The zero-shear-rate viscosity of the fluid is 13.6 Pa s, and the density is 880 kg/m^3. The surface tension of the polymeric solution is assumed to be equal to that of the polybutene solvent, which is quoted by the supplier as $\sigma = 0.03$ N/m. The four dimensionless groups (Re, We, g, De) are expressed in terms of these parameters and the rotation rate Ω (rad/s) as

$$Re = 1.618 \times 10^{-1} \times \Omega, \tag{29}$$

$$We = (2.818 \times 10^{-1})/\Omega^2, \tag{30}$$

$$g = (1.96 \times 10^{2})/\Omega^2, \tag{31}$$

$$De = 7.92 \times 10^{-1} \times \Omega. \tag{32}$$

The rheological parameters α and β, and the liquid volume V are independent of rotation rate. Steady solutions are computed for decreasing rotation rate for both the Newtonian and viscoelastic fluids and various values of V. The calculations are started with a high rotation rate ($\Omega \approx 4$ rad/s), at which the free surface is almost concentric with the cylinder and the rigid motion solution is a good first approximation for the field variables. The solution family that evolves with decreasing rotation rate is computed using arclength continuation, as described in §3.

The results are presented as plots of the arclength of the interface, normalized with the arclength of the circular surface that encloses the same volume, as a function of the rotation rate Ω. The normalized arclength represents the deviation of the interface from the shape for rigid rotation. Sample flow fields for specific values of Ω are also included.

4.2.1. *Newtonian flow*

The results in figures 7 and 8 are for a Newtonian fluid with the same properties as the Boger fluid, except $\lambda = 0$. The liquid volume per unit length used in these calculations is $V = 1.75$. The most important feature of these calculations is the occurrence of the limit point in rotation rate at $\Omega = \Omega_c \approx 2.53$ rad/s. No steady solutions were found for lower rotation rates and the family of flows turned back to higher values of Ω. As shown in figure 7(*a*), and in the expanded view figures 7(*b*), the limit point was computed with four finite-element meshes to guarantee that it is not an artifact of poor resolution of the flow field. The four meshes used each had uniform element sizes in the radial direction. The two meshes with $N_\theta = 60$ and 80

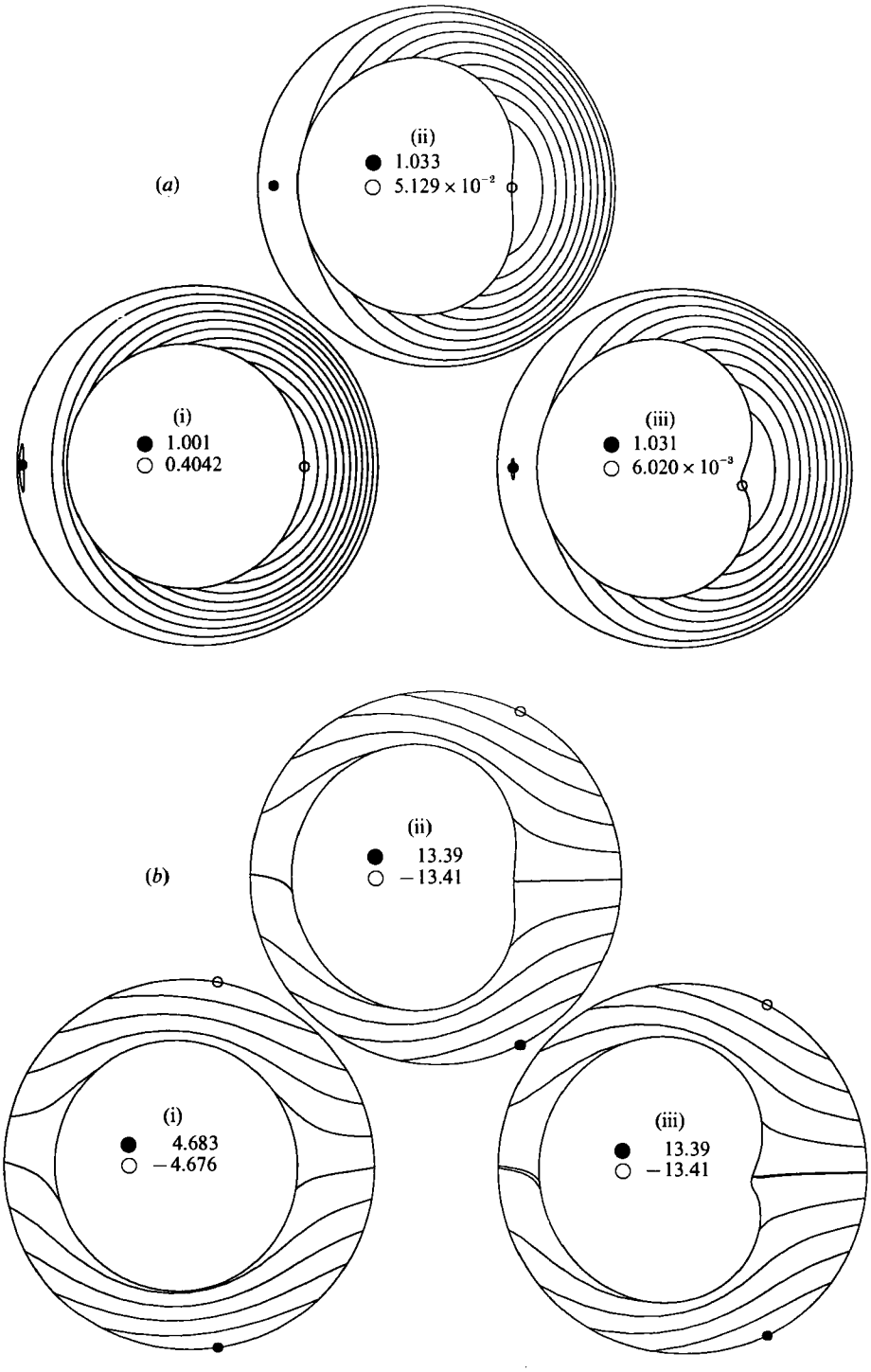

FIGURE 8. Contour plots of (*a*) azimuthal velocity (v_θ), and (*b*) pressure (p) calculated on a 40×10 mesh for a high-viscosity Newtonian fluid at three rotation rates (marked on figure 7): (i) 4.17 rad/s, (ii) 2.53 rad/s and (iii) 2.55 rad/s. Maximum (●) and minimum (○) values of the field are denoted.

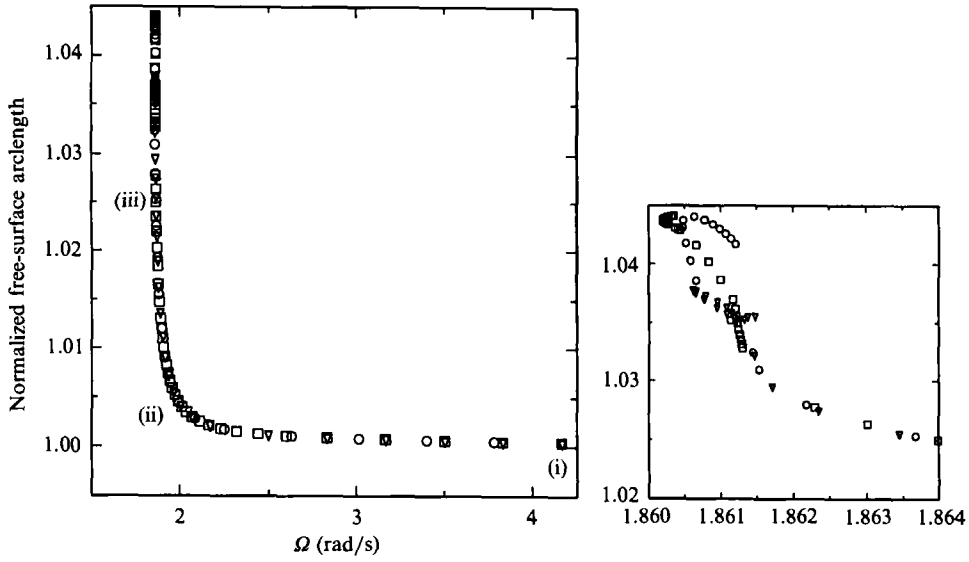

FIGURE 9. (*a*) Evolution of steady-state solution family for flow of a viscoelastic, Boger fluid ($\lambda = 0.792$ s) in a 0.05 m radius cylinder. (*b*) Expanded view near the limit-point value of the rotation rate point (iii) in (*a*). Meshes: □, 40×10; ▽, 60×10; ○, 80×10.

had elements concentrated azimuthally in the region of highest interface deformation near $\theta \approx -20°$.

Elementary ideas linking folds in solution curves in parameter space to the linear stability of each steady solution (Iooss & Joseph 1981) show that the flows on the reverse portion of the curve in figure 7 past the limit point must be temporally unstable. Then, the limit point must correspond to the minimum attainable rotation rate below which steady, two-dimensional, continuous films do not exist.

Sample interface shapes and fields for v_θ and p are shown in figure 8 for three values of Ω: (i) on the stable portion of the solution family, (ii) near the limit point, and (iii) on the unstable portion of the solution family. The interface on the stable side is almost a concentric circle with a slight displacement towards $\theta = \pi$. At the limit point, the interface is much flatter on the side of the cylinder with the rising flow. The interface for the unstable solution shows the formation of a bulge at $\theta \approx -20°$. The appearance of the bulge was the reason for the extensive mesh refinement in this part of the film.

It is interesting to follow the evolution of the maximum and minimum values of the azimuthal velocity as the solution evolves around the limit point. Between the high rotation rate (4 rad/s) and the limit point on the stable side of the family, the fluid decelerates on the rising side of the film, and the value of v_θ on the surface of the film at $\theta \approx 0$ decreases. The film thickens in this region to compensate for the slower motion. On the unstable part of the solution family, v_θ has almost dropped to zero in the bulge, indicating that the fluid is about to recirculate.

The bulging interface shapes are similar to some of the forms predicted by the lubrication analysis of Johnson (1988). However, he did not realize that these forms are unstable. The bulge is caused by the fluid stress normal to the interface exceeding the pressure in the gas phase. In order to compensate for this effect and maintain the force balance, the curvature must locally change sign to allow the surface force to act in the same direction as the gas pressure. The solution field near $\Omega \approx 2.55$ rad/s shows this bulging interface.

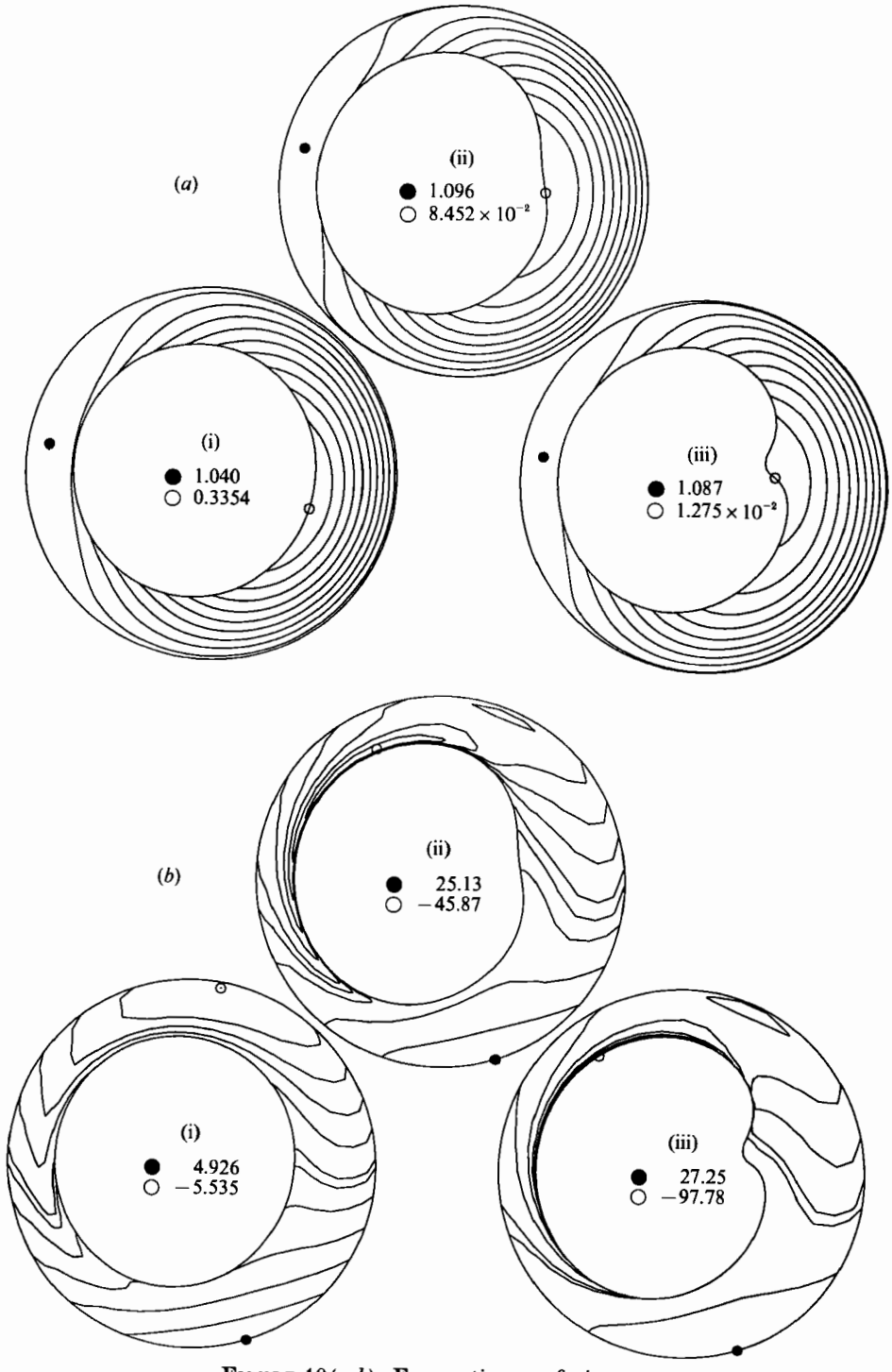

FIGURE 10(*a*, *b*). For caption see facing page.

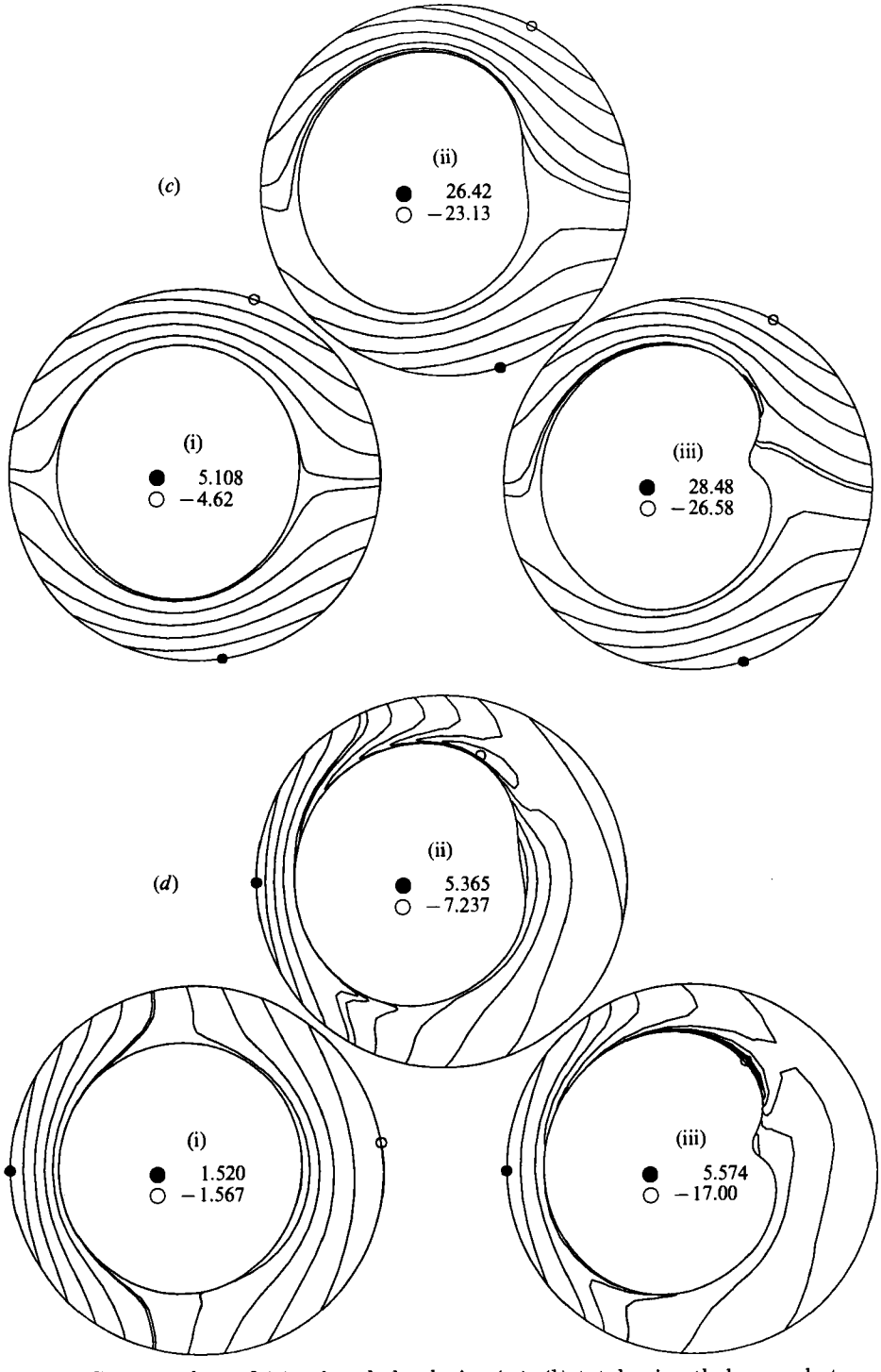

FIGURE 10. Contour plots of (*a*) azimuthal velocity (v_θ), (*b*) total azimuthal normal stress ($\pi_{\theta\theta}$), (*c*) total radial normal stress (π_{rr}) and (*d*) total shear stress ($\pi_{r\theta}$) calculated on a 40 × 10 mesh for a viscoelastic, Boger fluid ($\lambda = 0.792$ s) at three rotation rates: (i) 4.17 rad/s, (ii) 1.95 rad/s and (iii) 1.86 rad/s. Maximum (●) and minimum (○) values of the field are denoted.

Unfortunately, we were unable to continue the calculations to higher values of Ω along the unstable solution branch. Here, the bulge became so pronounced that the interface shape could not be represented as $r = h(\theta)$. Mathematically, this occurs when the interface becomes tangent to a spine emanating from the origin and $r = h(\theta)$ becomes multivalued. This tangency condition cannot be reached with this interface representation. Instead, another limit point is found and the discrete solution turns to lower rotation rates. This second limit point is an artifact of the failure of the interface representation. Solutions just beyond this point were not convergent with mesh refinement. Furthermore, the interface shapes computed in this region show sharp oscillations that are on the size of the mesh, indicative of a failure in the numerical method. Flows for higher rotation rates can only be computed using interface approximations that do not hinge on the Mongé representation.

The computations of Newtonian flows do not provide much motivation to adopt such a representation, because the bulging of the interface occurs on the unstable side of the family and would not be observable experimentally. However, the computations for the viscoelastic Boger fluid do provide this motivation.

4.2.2. *Viscoelastic flow*

All the calculations for viscoelastic flows were performed using meshes that were graded radially towards the free surface to capture the steep gradients in the azimuthal normal stress which appear there. In addition, the meshes with $N_\theta = 60$ and 80 were graded azimuthally to concentrate elements near the bulge which occurs near $\theta \approx 36°$. The normalized arclength of the interface computed as a function of Ω is shown in figure 9 for the Boger fluid with a volume per unit length $V = 1.75$. From an approximately concentric interface at $\Omega \approx 4$ rad/s, the interface flattens slightly on the rising side of the film without much change until $\Omega \approx 1.95$ rad/s. At this point, there is an increase in arclength as the same bulge observed for the Newtonian case develops. The bulge grows as Ω is decreased, but close to $\Omega \approx 1.86$ rad/s, it becomes too severe for the Mongé representation. No bifurcation or limit points are detected between $\Omega = 4$ and 1.86 rad/s. Thus, steady, viscoelastic flows exist at rotation rates well below the point where the Newtonian flows cease to exist and turn back to higher rotation rates. Furthermore, the bulging interface shapes are found on the stable branch of the solution family.

Sample fields for the variables (v_θ, $\pi_{\theta\theta}$, π_{rr}, $\pi_{r\theta}$) are shown in figure 10 for the rotation rates corresponding to the three points (i)–(iii) shown in figure 9(*a*). The trends in the maximum and minimum values of the azimuthal velocity are the same as those observed for the Newtonian flow. The stress fields give some indication of why steady, viscoelastic flows exist at lower rotation rates. As the analysis in §5 reveals, the Newtonian limit point is a consequence of gravity overcoming the viscous drag of the cylinder. From the contours of v_θ near the Newtonian limit point (figure 8*a*), the shear stress at $(r, \theta) \approx (1, 0)$ is $\pi_{r\theta} \approx -2$. From the plot of shear stress for the viscoelastic case (figure 10*d*, ii), the shear stress in the same region of the flow is twice as large, which is indicative of greater drag on the fluid. Hence, the rotation rate at which gravity can overcome the drag force of the cylinder is shifted to lower values, and steady solutions exist at lower rotation rates, as compared to the Newtonian case.

The limit point in Ω for the Boger fluid could not be computed because of the failure of the Mongé interface representation. In order to establish whether this limit point exists for a viscoelastic fluid, we simulated the flow of a viscoelastic fluid

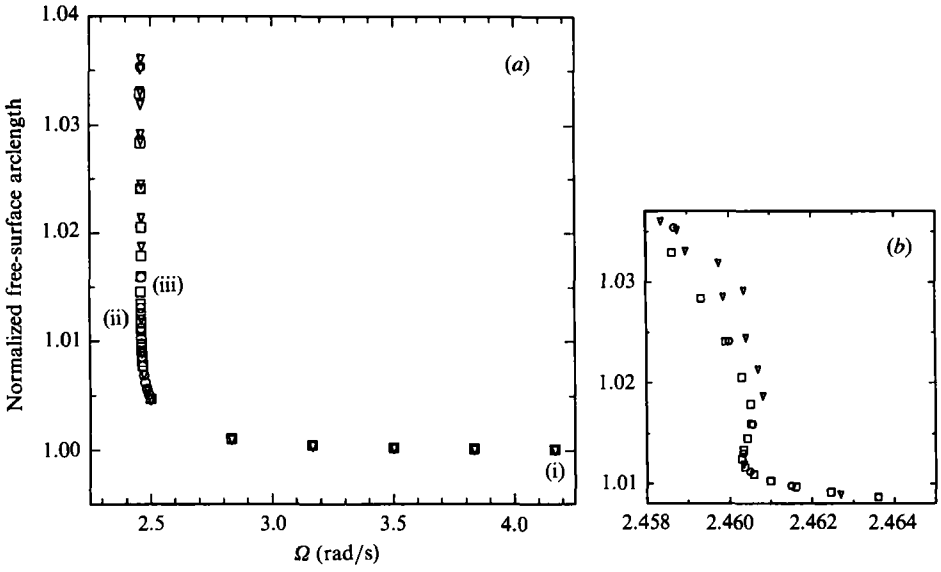

FIGURE 11. (*a*) Evolution of the steady-state solution family for flow of a viscoelastic, Boger fluid ($\lambda = 0.132$ s) in a 0.05 m radius cylinder. (*b*) Expanded view near the limit-point value of the rotation rate, point (ii) in (*a*). Meshes: □, 40 × 10; ▽, 60 × 10; ○, 80 × 10.

identical to the Boger fluid in all its properties, except that the fluid time constant was lowered to $\lambda = 0.132$ s, or one-sixth of the value for the Boger fluid. The results of this simulation are shown in figures 11 and 12 for a liquid volume per unit length $V = 1.75$. The limit point is observed at a rotation rate of $\Omega_c \approx 2.46$ rad/s and is convergent with mesh refinement. Thus, even with a less elastic fluid, steady solutions exist at lower rotation rates than for the Newtonian fluid. For $\lambda =$ 0.132 s, just around the limit point, the arclength increases rapidly, the bulge develops, and the interface representation breaks down.

There are some other interesting effects of viscoelasticity. For example, introducing viscoelasticity rotates the bulging section of the interface to higher values of θ relative to the Newtonizn flow. The bulge appears at approximately $\theta = -20°$ for the Newtonian case and $\theta = 36°$ for the Boger fluid. This phase shift is a manifestation of the delayed response of a viscoelastic fluid to an imposed strain rate, compared to the instantaneous response of Newtonian fluids. The larger the fluid time constant, the longer it takes the fluid to respond to any imposed strain rate and the greater the magnitude of the counterclockwise phase shift in rimming flow.

The extensional behaviour of viscoelastic fluids is accentuated by the two viscoelastic simulations with different time constants. While the kinematics are essentially the same in both flows, the azimuthal normal stresses show dramatically different behaviour. For the higher time constant, steep gradients in $\pi_{\theta\theta}$ build up near the free surface, as seen by the collapsing of the contours on the free surface in figure 10(*b*). The simulations with the lower time constant do not show steep gradients in $\pi_{\theta\theta}$ anywhere in the domain. These differences are explained on the basis of the extensional properties of the fluid. A fluid element close to the interface experiences an appreciable extension rate ($\approx (1/r)\,\partial v_\theta/\partial\theta$) as it moves between $0 \leqslant \theta \leqslant \pi$. This is evident from figure 13 which shows streamlines superimposed on contours of azimuthal velocity at $\Omega = 1.86$ rad/s, for $\lambda = 0.792$ s. The Giesekus model predicts a rapid increase in the extensional viscosity at a critical value of extension rate that is inversely proportional to the time constant. The increase in extensional viscosity

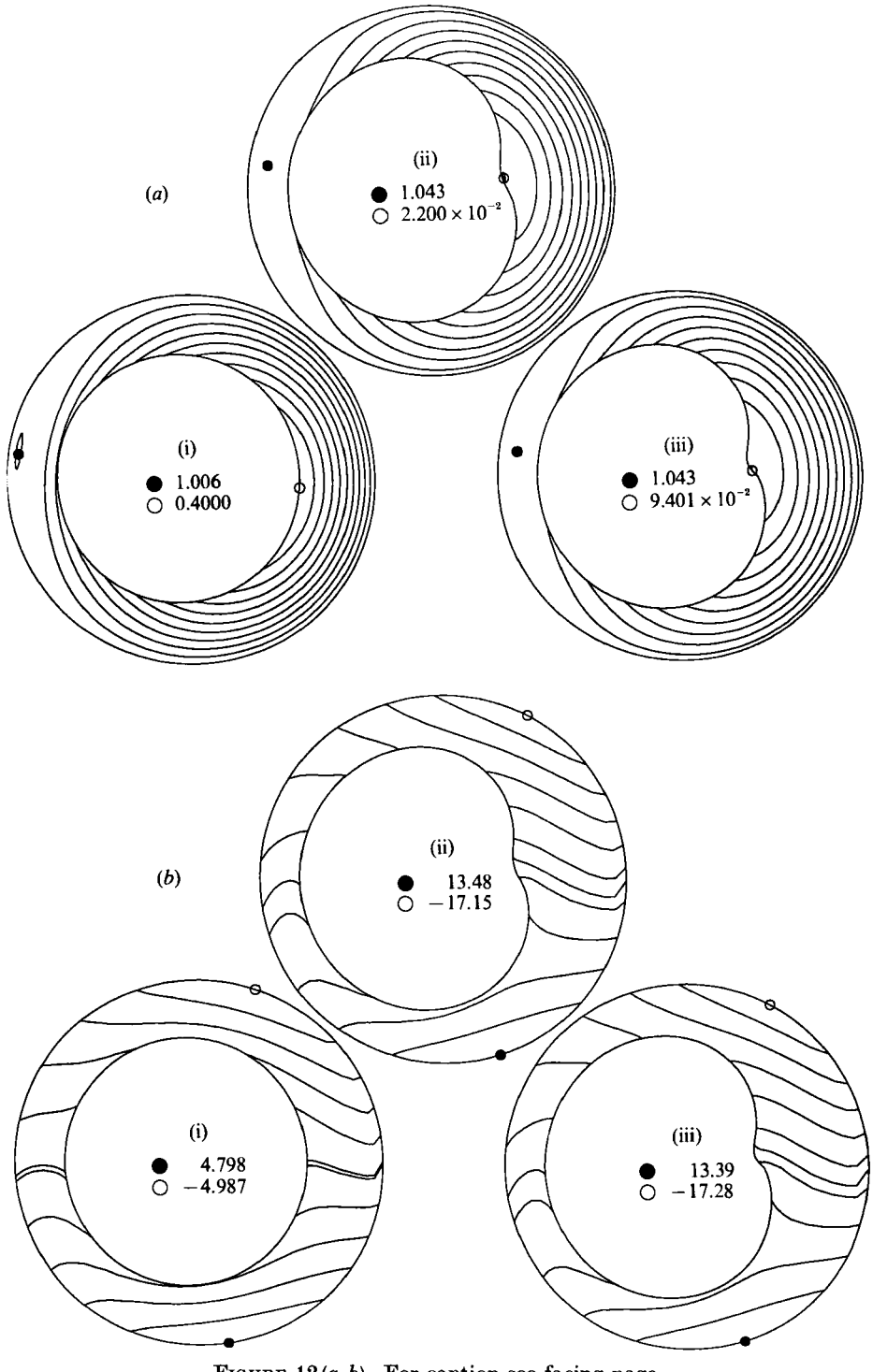

FIGURE 12(*a*, *b*). For caption see facing page.

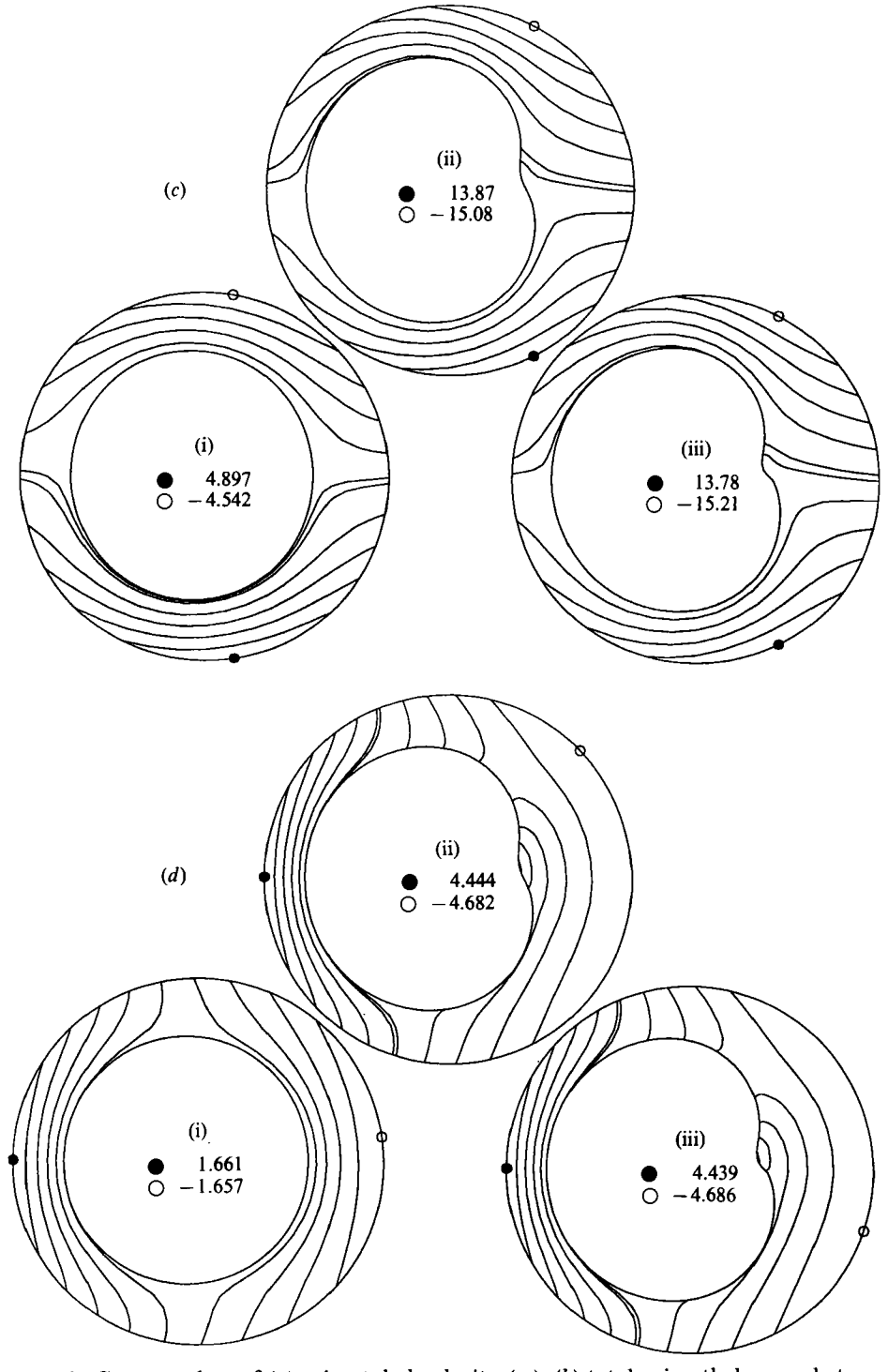

FIGURE 12. Contour plots of (*a*) azimutyhal velocity (v_θ), (*b*) total azimuthal normal stress ($\pi_{\theta\theta}$), (*c*) total radial normal stress (π_{rr}) and (*d*) total shear stress ($\pi_{r\theta}$) calculated on a 40×10 mesh for a viscoelastic, Boger fluid ($\lambda = 0.132$ s) at three rotation rates: (i) 4.17 rad/s, (ii) 2.4603 rad/s and (iii) 2.4605 rad/s. Maximum (●) and minimum (○) values of the field are denoted.

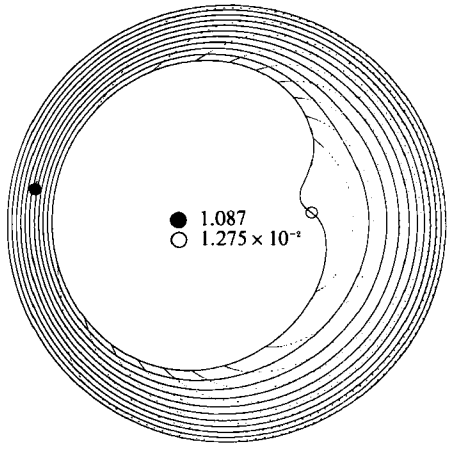

FIGURE 13. Streamlines (solid lines) superimposed on contours of azimuthal velocity (dashed lines) calculated on a 40×10 mesh for a viscoelastic, Boger fluid ($\lambda = 0.792$ s) at a rotation rate $\Omega = 1.86$ rad/s. Maximum (●) and minimum (○) values of the field are denoted.

is proportional to $1/\alpha$. For the higher time constant, the critical extension rate is below the extension rate in the flow, so that the viscosity increase leads to stress build-up at the interface. Conversely, the critical extension rate for the fluid with the lower time constant is not attained in the flow and no dramatic increase is observed in $\pi_{\theta\theta}$.

5. Lubrication analysis

The liquid films reported in the calculations shown in figure 8 suggest that a lubrication theory based on the assumption that the average film thickness ϵ (scaled with R_c) is small may describe the nonlinear behaviour described in §4.2. We have developed such an asymptotic theory for Newtonian flows; our analysis is similar to the theory reported by Johnson (1988). The general approach we follow is similar to the one used by Babchin *et al.* (1983) to derive the Kuramoto–Sivashinsky equation describing the interfacial deformation associated with the Rayleigh–Taylor instability. We begin by defining a dimensionless coordinate y as

$$r \equiv 1 - \epsilon y. \tag{33}$$

In addition, the position of the interface in wall coordinates $\psi = \psi(\theta)$ is defined as

$$h \equiv 1 - \epsilon\psi. \tag{34}$$

Both y and ψ are scaled by the average film thickness ϵ and are $O(1)$ for $\epsilon \ll 1$.

The lubrication approximation is formed by scaling the governing equations (3)–(6), the boundary conditions (12)–(15), and the volume constraint (16) so that $\epsilon \ll 1$ and $\epsilon^2 Re \leqslant 1$. The continuity equation (3) and the $r-$ and $\theta-$components of the momentum equation become

$$\frac{\partial v_r}{\partial y} = \frac{\partial v_\theta}{\partial \theta}, \tag{35}$$

$$\frac{\partial \mathscr{P}}{\partial y} = 0, \tag{36}$$

$$\frac{\partial^2 v_\theta}{\partial y^2} - \frac{\partial \mathscr{P}}{\partial \theta} = 0, \tag{37}$$

where the reduced pressure $\mathscr{P}(y, \theta)$ is defined by

$$\nabla\mathscr{P} \equiv \epsilon^2 Re\,(\nabla p - g\boldsymbol{j} - r\boldsymbol{e}_r). \tag{38}$$

The boundary conditions (12)–(15) reduce to

$$v_\theta = 1, \quad y = 0, \tag{39}$$

$$v_r = -\frac{\mathrm{d}\psi}{\mathrm{d}\theta} v_\theta, \quad y = \psi, \tag{40}$$

$$\frac{\partial u_\theta}{\partial y} = 0, \quad y = \psi, \tag{41}$$

and

$$p - p_g = -2\mathscr{H} We. \tag{42}$$

Finally, the volume constraint (16) is written as

$$\frac{1}{2\pi}\int_0^{2\pi} \psi \,\mathrm{d}\theta = 1. \tag{43}$$

Equation (36) implies $\mathscr{P} \equiv \mathscr{P}(\theta)$, and (37) is integrated twice to give

$$v_\theta = 1 + \frac{\mathrm{d}\mathscr{P}}{\mathrm{d}\theta}\left(\frac{y^2}{2} - y\psi\right), \tag{44}$$

where the constants of integration have been evaluated from (39) and (41). The continuity equation (35) is integrated to yield $v_r(y, \theta)$, and the two components of $\boldsymbol{v}$ are substituted into (40) to give

$$\frac{1}{3}\frac{\mathrm{d}^2\mathscr{P}}{\mathrm{d}\theta^2}\psi^3 + \frac{\mathrm{d}\mathscr{P}}{\mathrm{d}\theta}\frac{\mathrm{d}\psi}{\mathrm{d}\theta}\psi^2 - \frac{\mathrm{d}\psi}{\mathrm{d}\theta} = 0. \tag{45}$$

Integration of (45) yields

$$\psi - \frac{1}{3}\frac{\mathrm{d}\mathscr{P}}{\mathrm{d}\theta}\psi^3 = 1, \tag{46}$$

where the constant of integration has been set equal to unity so that ψ is identically equal to the average film thickness in the limit of solid-body rotation, i.e. $\mathrm{d}\mathscr{P}/\mathrm{d}\theta = 0$. It remains to relate the pressure derivative in (46) to ψ. This is done using the normal stress condition (42) and the definition (38), which together yield

$$\frac{\mathrm{d}\mathscr{P}}{\mathrm{d}\theta} = \epsilon^2 Re\left(-2We\frac{\mathrm{d}\mathscr{H}}{\mathrm{d}\theta} + g\cos\theta\right). \tag{47}$$

Writing $\mathrm{d}\mathscr{H}/\mathrm{d}\theta$ in terms of ψ and substituting into (46) gives the following nonlinear, ordinary differential equation for ψ:

$$\psi - \tfrac{1}{3}\psi^3\epsilon^2 Re\,[2\epsilon We(\psi''' - \psi') + g\cos\theta] = 1, \tag{48}$$

where a prime denotes a derivative with respect to θ. Equation (48) governs the interface position. In the limit $We \to 0$, it is equivalent to the expression recently derived by Johnson (1988), in which surface tension was neglected.

5.1. *Perturbation analysis for small g*

A solution valid in the limit $g \ll 1$ is obtained by deriving a regular perturbation expansion as

$$\psi = \psi_0 + \psi_1 g + \psi_2 g^2 + \ldots. \tag{49}$$

ϵ	(i)	(ii)	(iii)	FEM
0.05	0.0793	0.0793	0.117	0.140
0.10	0.317	0.317	0.467	0.483
0.20	1.27	1.27	1.87	1.415
0.33	3.53	3.53	5.20	2.53

TABLE 1. Values of Ω(rad/s) at the limit point.

The equations that govern the coefficients $(\psi_0, \psi_1, \ldots)$ are obtained by substituting (49) into (48) and collecting terms of equal order in g. The solutions to the two lowest order problems that satisfy (43) and the periodic boundary conditions are

$$\psi_0 = 1 \tag{50}$$

and

$$\psi_1 = \frac{\frac{1}{3}\epsilon^2 Re}{1+(\frac{4}{3}\epsilon^3 Re\, We)^2}\cos\theta + \frac{\frac{4}{9}\epsilon^5 Re^2 We}{1+(\frac{4}{3}\epsilon^3 Re\, We)^2}\sin\theta. \tag{51}$$

For any case other than $We \gg 1$, the conditions assumed in applying the lubrication approximation require that (51) be equivalent to

$$\psi_1 \equiv \frac{1}{3}\epsilon^2 Re\cos\theta, \tag{52}$$

which is identical to the result given by Ruschak & Scriven (1976).

5.2. *Spectral analysis*

The nonlinear behaviour of (48) is examined by representing the solution in the Fourier series

$$\psi = 1 + \sum_{n=1}^{N_a} A_n \cos n\theta + \sum_{n=1}^{N_b} B_n \sin n\theta. \tag{53}$$

Setting the first term of the right side of (53) equal to unity ensures that (43) is satisfied. Substituting (53) into (48) and applying Galerkin's method yields a set of (N_a+N_b) nonlinear, algebraic equations for the remaining coefficients (A_n, B_n). The solution of this set of algebraic equations is compared below with the numerical calculations presented in §4.

Three levels of approximation have been studied: (i) $N_a = 1$ and $N_b = 0$, (ii) $N_a = 1$ and $N_b = 1$, and (iii) $N_a = 2$ and $N_b = 2$. For case (i), two solutions for A_1 are readily obtained as

$$A_1 = \frac{1 \pm [1-(\epsilon^2 Re\, g)^2]^{\frac{1}{2}}}{\frac{3}{2}\epsilon^2 Re\, g}. \tag{54}$$

In the limit $\epsilon^2 Re\, g \ll 1$, the asymptotic result (52) is obtained directly from (54). The two real solutions given by (54) become complex at a limit point given by

$$\epsilon^2 Re\, g = 1, \tag{55}$$

which confirms the predictions of a limit point reported in §4.

The spectral approximations (ii) and (iii) yield two and four nonlinear algebraic equations, respectively, which are solved numerically and which also exhibit limit-point behaviour. The limit points in Ω predicted by the approximations (i), (ii), and (iii) are compared in table 1 with the finite-element results method of §3 for the parameter values given in (29)–(31). As expected, the two sets of results are in better agreement as ϵ becomes small and as N_a and N_b are increased.

As a further comparison between the lubrication theory and the computations, we have evaluated the Fourier coefficients from the finite-element solutions and have compared these directly to the results of the lubrication approximation (iii) (see table 2). The comparison is made for two rotation rates at $\epsilon = 0.1$ and 0.2. The agreement for the coefficients A_1 and A_2 is quite good, even at the lower rotation rate, which is close to the limit point in Ω. For each case, the values of B_1 and B_2 are negligible compared to A_1 and A_2, suggesting that the contribution of the sine terms in (53) is negligible at these parameter values. This result is consistent with the perturbation approximation (51), where the cosine terms dominate if $We \ll g$. The agreement between the numerical and analytical values of the coefficients B_1 and B_2 is not as good.

The simplicity of the result (55) leads to a straightforward physical explanation for the presence of a limit point with decreasing rotation rate. The dimensionless product gRe is a measure of the relative importance of gravitational and viscous forces. Equation (55) implies that the viscous forces must dominate the gravitational forces by an amount that scales as $1/\epsilon^2$ for a stable fluid layer to exist. Beyond this limit, gravity will cause the fluid to gather at the bottom of the cylinder more rapidly than it is carried upward by viscous forces exerted by the cylinder wall. Violating this balance results in a partial, or incomplete coating. Interestingly, the effects of surface tension are not important at the parameter values given in (29)–(32), and need not be included in the calculation of limit points such as those described here.

6. Discussion

Our calculations for the rimming flow of Newtonian and viscoelastic fluids demonstrate the accuracy and stability of the elastic–viscous split stress (EVSS)/ finite-element method (FEM) for solving viscoelastic, free-surface flows, without contact-line singularities. The calculations converge with mesh refinement and capture the steep boundary layers in the stress field that develop with increasing fluid elasticity and deviation from rigid-body motion.

Even the relatively simple geometry of the rimming flow poses significant difficulties for numerical simulation. First, continuous liquid films do not exist for all rotation rates. The appearance of limiting values of the rotation rate is demonstrated, below which the family of steady, two-dimensional flows reverses direction and continues to higher values of Ω. This limit point in rotation rate marks the end of the existence of steady, two-dimensional flows. Unless the film is destabilized by steady, three-dimensional or time-periodic, two-dimensional flow transitions at higher rotation rates, this limit point also corresponds to the stability boundary for these flows. The limited experimental data of Sanders *et al.* (1981) lead us to suspect that three-dimensional transitions may play a role in the stability of these films. For thin liquid films, the limiting value of Ω is well predicted by the analysis of the nonlinear, film-flow equation derived from lubrication theory. This theory clearly demonstrates that the loss of solution is a result of the competition between gravity and viscous forces. The lubrication theory predicts the limit point for thicker films, but the agreement with the numerical simulations deteriorates substantially. Interestingly, the film shapes beyond the limit point show the development of a bulge in the ascending part of the flow. These unstable films resemble the distorted forms predicted by Johnson (1988), but which were not previously linked to the occurrence of the minimum rotation rate.

Adding elasticity to the fluid, by increasing the relaxation time from zero, leads to

	$\epsilon = 0.1$			
	$\Omega = 8.33$ rad/s		$\Omega = 0.542$ rad/s	
	(iii)	FEM	(iii)	FEM
A1	1.27×10^{-2}	1.18×10^{-2}	2.53×10^{-1}	2.22×10^{-1}
B1	9.30×10^{-8}	6.00×10^{-5}	8.46×10^{-5}	-3.28×10^{-5}
A2	2.42×10^{-4}	1.18×10^{-4}	8.94×10^{-2}	6.92×10^{-2}
B2	1.23×10^{-8}	2.55×10^{-6}	1.08×10^{-4}	-2.22×10^{-5}
	$\epsilon = 0.2$			
	$\Omega = 8.33$ rad/s		$\Omega = 1.92$ rad/s	
	(iii)	FEM	(iii)	FEM
A1	5.13×10^{-2}	4.20×10^{-2}	3.48×10^{-1}	2.09×10^{-1}
B1	3.21×10^{-6}	7.73×10^{-4}	4.45×10^{-3}	9.15×10^{-4}
A2	3.94×10^{-3}	1.78×10^{-3}	1.59×10^{-1}	4.47×10^{-2}
B2	1.64×10^{-6}	7.95×10^{-5}	5.88×10^{-4}	4.35×10^{-4}

TABLE 2. Comparison of surface shapes computed from the spectral expansion and the finite-element method

the existence of steady flows at lower rotation rates. For the parameters of the Boger fluid described in §4.2, adding a relaxation time of less than 1 s leads to the existence of steady flows at almost 1 rad/s below the critical rotation rate for Newtonian flows. The increased range of rotation rates for the existence of viscoelastic flows results from the appreciably higher drag exerted on the fluid as a consequence of elasticity. In addition, elasticity stabilizes the bulging interface shapes. The bulges lead to almost stagnant flow near the interface in the thickest part of the film and should be observable in experiments.

The maximum value of the fluid relaxation time that can be used in the EVSS/FEM calculations is not limited by the numerical discretization, but by the bulge in the interface, which causes the Mongé representation of the interface to fail. Continuing the calculations to larger relaxation times and rotation rates further along the solution families will require a more general interface representation. We are investigating the use of elliptic mesh generation techniques (Ryskin & Leal 1983; Christodoulou and Scriven 1992; Tsiveriotis & Brown 1991) for this purpose.

We are grateful to the National Science Foundation and the Office of Naval Research for their financial support of this research. Computational resources were supplied by a grant from the Pittsburgh National Supercomputer Center.

REFERENCES

APELIAN, M. R., ARMSTRONG, R. C. & BROWN, R. A. 1988 Impact of the constitutive equation and singularity on the calculation of stick-slip flow: the modified upper-convected Maxwell model (MUCM). *J. Non-Newtonian Fluid Mech.* **27**, 299–321.

BABCHIN, A. J., FRENKEL, A. L., LEVICH, B. G. & SIVASHINSKY, G. I. 1983 Nonlinear saturation of Rayleigh–Taylor instability in thin films. *Phys. Fluids* **26**, 3159–3161.

BIRD, R. B., ARMSTRONG, R. C. & HASSAGER, O. 1987 *Dynamics of Polymeric Liquids, Vol. I, Fluid Mechanics.* John Wiley.

BOUSFIELD, D. W., KEUNINGS, R., MARUCCI, G. & DENN, M. M. 1986 Non-linear analysis of

surface tension driven breakup of viscoelastic filaments. *J. Non-Newtonian Fluid Mech.* **21**, 79–97.

BROOKS, A. N. & HUGHES, T. J. R. 1982 Streamline upwind/Petrov–Galerkin formulation for convection dominated flows with particular emphasis on the incompressible Navier–Stokes equations. *Comput. Meth. Appl. Mech. Engng* **32**, 199–259.

BROWN, R. A., ARMSTRONG, R. C., BERIS, A. N. & YEH, P.-W. 1986 Galerkin finite element analysis of complex viscoelastic flows. *Comput. Meth. Appl. Mech. Engng* **58**, 201–226.

BURDETTE, S. R., COATES, P. J., ARMSTRONG, R. C. & BROWN, R. A. 1989 Calculations of viscoelastic flow through an axisymmetric corrugated tube using the explicitly elliptic momentum equation formulation (EEME). *J. Non-Newtonian Fluid Mech.* **33**, 1–23.

CAREY, G. F. & ODEN, J. T. 1986 *Finite Elements: Fluid Mechanics Vol. VI.* Prentice-Hall.

CHRISTODOULOU, K. N. & SCRIVEN, L. E. 1992 Discretization of free surface flows and other moving boundary problems. *J. Comput. Phys.* (in press).

COATES, P. J., ARMSTRONG, R. C. & BROWN, R. A. 1992 Calculation of steady viscoelastic flow through axisymmetric contractions using the EEME formulation. *J. Non-Newtonian Fluid Mech.* (in press).

CROCHET, M. J., DAVIES, A. R. & WALTERS, K. 1984 *Numerical Simulation of Non-Newtonian Flow.* Elsevier.

CROCHET, M. J., DELVAUX, V. & MARCHAL, M. J. 1990 On the convergence of the streamline-upwind mixed finite element. *J. Non-Newtonian Fluid Mech.* **34**, 261–268.

DEIBER, J. A. & CERRO, R. L. 1976 Viscous flow with a free surface inside a horizontal rotating drum. I. hydrodynamics. *Indust. Engng Chem. Fundam.* **15**, 102–110.

DHEUR, J. & CROCHET, M. J. 1989 stratified flows of newtonian and viscoelastic fluids. *J. Non-Newtonian Fluid Mech.* **32**, 1–18.

GIESEKUS, H. 1982 A simple constitutive equation for polymer fluids based on the concept of deformation dependent tensorial mobility. *J. Non-Newtonian Fluid Mech.* **11**, 69–109.

GREEN, A. E. & RIVLIN, R. S. 1957 The mechanics of non-linear materials with memory, Part I. *Arch. Rat. Mech. Anal.* **1**, 1–21.

HOOD, P. 1976 Frontal solution program for unsymmetric matrices. *Intl J. Numer. Meth. Engng* **10**, 379–399.

IOOSS, G. & JOSEPH, D. D. 1981 *Elementary Stability and Bifurcation Theory.* Springer.

JOHNSON, C., NAVERT, U. & PITKARANTA, J. 1984 Finite element methods for linear hyperbolic problems. *Comput. Meth. Appl. Mech. Engng* **45**, 285–312.

JOHNSON, R. E. 1988 Steady-state coating flows inside a rotating horizontal cylinder. *J. Fluid Mech.* **190**, 321–342.

JOSEPH, D. D., RENARDY, M. & SAUT, J.-C. 1985 Hyperbolicity and change of type in the flow of viscoelastic fluids. *Arch. Rat. Mech. Anal.* **87**, 213–251.

KARWEIT, M. J. & CORRSIN, S. 1975 Observations of cellular patterns in a partly filled, horizontal rotating drum. *Phys. Fluids* **18**, 111–112.

KEUNINGS, R. 1986 An algorithm for the simulation of transient viscoelastic flows with free surfaces. *J. Comput. Phys.* **62**, 199–220.

KEUNINGS, R. 1989 Simulation of viscoelastic fluid flow. In *Fundamental of Computer Modeling for Polymer Processing* (ed. C. L. Tucker), 403–469. Carl Hanser.

KEUNINGS, R. & BOUSFIELD, D. W. 1987 Analysis of surface tension driven leveling in viscoelastic flows. *J. Non-Newtonian Fluid Mech.* **22**, 219–233.

KING, R. C., APELIAN, M. R., ARMSTRONG, R. C. & BROWN, R. A. 1988 Numerically stable finite element techniques for viscoelastic calculations in smooth and singular geometries. *J. Non-Newtonian Fluid Mech.* **29**, 147–216.

KISTLER, S. F. & SCRIVEN, L. E. 198 Coating flows. In *Computational Analysis of Polymer Processing* (eds J. R. A. Pearson & S. M. Richardson), p. 243. Essex: Applied Science Publishers.

MARCHAL, J. M. & CROCHET, M. J. 1987 A new mixed finite element method for calculating viscoelastic flow. *J. Non-Newtonian Fluid Mech.* **26**, 77–114.

MUSARRA, S. & KEUNINGS, R. 1989 Co-current exisymmetric flow in complex geometries: Numerical simulation. *J. Non-Newtonian Fluid Mech.* **32**, 253–268.

NORTHEY, P. J., ARMSTRONG, R. C. & BROWN, R. A. 1990 Finite-element calculation of time-dependent two-dimensional viscoelastic with the EEME formulation. *J. Non-Newtonian Fluid Mech.* **36**, 109–133.

ORR, F. M. & SCRIVEN, L. E. 1978 Rimming flow: numerical simulation of steady, viscous, free-surface flow with surface tension. *J. Fluid Mech.* **84**, 145–165.

PEARSON, J. R. A. 1985 *Mechanics of Polymer Processing.* Elsevier.

PILITSIS, S. & BERIS, A. N. 1989 Calcaulations of steady-state viscoelastic flow in an undulating tube. *J. Non-Newtonian Fluid Mech.* **31**, 231–287.

QUINZANI, L. M., MCKINLEY, G. H., BROWN, R. A. & ARMSTRONG, R. C. 1990 Modeling the rheology of polyisobutylene solutions. *J. Rheol.* **34**, 705–748.

RAJAGOPALAN, D., ARMSTRONG, R. C. & BROWN, R. A. 1990*a* Calculation of steady viscoelastic flow using a multimode maxwell model: application of the explicitly elliptic momentum equation (EEME) formulation. *J. Non-Newtonian Fluid Mech.* **36**, 135–158.

RAJAGOPALAN, D., ARMSTRONG, R. C. & BROWN, R. A. 1990*b* Finite element methods for calculation of steady, viscoelastic flow using constitutive equations with a Newtonian viscosity. *J. Non-Newtonian Fluid Mech.* **36**, 159–193.

RAO, M. A. & THORNE, J. L. 1972 Principles of rotational moulding. *Polymer. Engng Sci.* **12**, 237–264.

RUSCHAK, K. J. & SCRIVEN, L. E. 1976 Rimming flow of liquid in a rotating horizontal cylinder. *J. Fluid Mech.* **76**, 113–125.

RYSKIN, G. & LEAL, L. G. 1983 Orthogonal mapping. *J. Comput. Phys.* **50**, 71–100.

SACKINGER, P. A., BROWN, R. A. & DERBY, J. J. 1989 A finite element method for analysis of fluid flow, heat transfer and free interfaces in Czochralski crystal growth. *Intl J. Numer. Meth. Fluids* **9**, 453–492.

SANDERS, J., JOSEPH, D. D. & BEAVERS, G. S. 1981 Rimming flow of a viscoelastic liquid inside a rotating horizontal cylinder. *J. Non-Newtonian Fluid Mech.* **9**, 269–300.

STRANG, G. & FIX, G. F. 1973 *An Analysis of the Finite Element Method.* Prentice-Hall.

TSIVERIOTIS, K. G. & BROWN, R. A. 1991 Boundary conforming mapping applied to computations of highly deformed solidification interfaces. *Intl J. Numer. Meth. Fluids* (in press).

WEATHERBURN, C. E. 1927 *Differntial Geometry of Three Dimensions.* Cambridge University Press.

YAMAGUCHI, Y., CHANG, C. J. & BROWN, R. A. 1984 Multiple buoyancy driven flow in a vertical cylinder heated from below. *Phil. Trans. R. Soc. Lond.* A**312**, 519–552.